PHYSICS OF FLUIDS **29**, 052001 (2017)

Effects of heat sink and source and entropy generation on MHD mixed convection of a Cu-water nanofluid in a lid-driven square porous enclosure with partial slip

A. J. Chamkha,[1,2] A. M. Rashad,[3] M. A. Mansour,[4] T. Armaghani,[5,a] and M. Ghalambaz[6]
[1]*Mechanical Engineering Department, Prince Mohammad Bin Fahd University, Al-Khobar 31952, Kingdom of Saudi Arabia*
[2]*Prince Sultan Endowment for Energy and Environment, Prince Mohammad Bin Fahd University, Al-Khobar 31952, Kingdom of Saudi Arabia*
[3]*Department of Mathematics, Faculty of Science, Aswan University, Aswan 81528, Egypt*
[4]*Department of Mathematics, Faculty of Science, Assuit University, Assuit, Egypt*
[5]*Department of Engineering, Mahdishahr Branch, Islamic Azad University, Mahdishahr, Iran*
[6]*Department of Mechanical Engineering, Dezful Branch, Islamic Azad University, Dezful, Iran*

(Received 8 May 2016; accepted 31 March 2017; published online 1 May 2017)

In this work, the effects of the presence of a heat sink and a heat source and their lengths and locations and the entropy generation on MHD mixed convection flow and heat transfer in a porous enclosure filled with a Cu-water nanofluid in the presence of partial slip effect are investigated numerically. Both the lid driven vertical walls of the cavity are thermally insulated and are moving with constant and equal speeds in their own plane and the effect of partial slip is imposed on these walls. A segment of the bottom wall is considered as a heat source meanwhile a heat sink is placed on the upper wall of cavity. There are heated and cold parts placed on the bottom and upper walls, respectively, while the remaining parts are thermally insulated. Entropy generation and local heat transfer according to different values of the governing parameters are presented in detail. It is found that the addition of nanoparticles decreases the convective heat transfer inside the porous cavity at all ranges of the heat sink and source lengths. The results for the effects of the magnetic field show that the average Nusselt number decreases considerably upon the enhancement of the Hartmann number. Also, adding nanoparticles to a pure fluid leads to increasing the entropy generation for all values of D for $\lambda_l = -\lambda_r = 1$. *Published by AIP Publishing.* [http://dx.doi.org/10.1063/1.4981911]

NOMENCLATURE

B = Dimensionless heat source, b/H
B_0 = Magnetic field strength, *T*
Be = Bejan number
b = Length of heat source, *m*
C_p = Specific heat, $J\ kg\ K^{-1}$
D = Dimensionless heat source position
Da = Darcy number, $Da = K/H^2$
d = Location of heat sink and source, m
H = Length of cavity, *m*
Ha = Hartmann number, $B_0 L\sqrt{\sigma_f/\rho_f \nu_f}$
K = Permeability of porous medium, m^2
k = Thermal conductivity, W m^{-1} K^{-1}
N = slip constant
Nu = Local Nusselt number, hH/k
Nu_m = Average Nusselt number of heat source
p = Fluid pressure, *Pa*
P = Dimensionless pressure, $P = \frac{p}{\rho_{nf} V_0^2}$
Pr = Prandtl number, ν_f/α_f,
Q_0 = Heat generation coefficient, W m^{-2}
Ra = Rayleigh number, $g\beta_f\,(T_h - T_c)\,H^3/\alpha_f\vartheta_f$
Ri = Richardson number, $Ri = Gr/\mathrm{Re}^2$
S = Entropy generation, W K^{-1} m^{-3}
S_1, S_r = Dimensionless partial slip parameters,
T = Temperature, *K*
T_0 = Reference temperature $(T_h + T_c)/2$
T_c = Cold wall temperature, *K*
T_h = Heated wall temperature, *K*
u, *v* = Velocity components in x, y directions, m s^{-1}
u = Velocity vector
U, V = Dimensionless velocity components, u/V_0, v/V_0
V_0 = Lid velocity m s^{-1}
x, y = Cartesian coordinates, *m*
X, Y = Dimensionless coordinates, *x/L*, *y/L*

Greek symbols

α = Thermal diffusivity, m^2 s^{-1}, $k/\rho c_p$
β = Thermal expansion coefficient, K^{-1}
ϕ = Solid volume fraction
σ = Effective electrical conductivity, s m^{-1}
θ = Dimensionless temperature, $(T - T_c)/(T_h - T_C)$
μ = Dynamic viscosity, N s m^{-2}
λ = Constant moving parameter
ν = Kinematic viscosity, m^2 s^{-1}
ρ = Density, kg m^{-3}
ε = Porosity

---

[a] armaghani.taher@yahoo.com

1070-6631/2017/29(5)/052001/22/$30.00

Subscripts

c = Cold
0 = Reference
f = Pure fluid
h = Hot
m = Average
nf = Nanofluid
p = Nanoparticle
s = Porous matrix
r = Right
l = Left

Vectors

J = Electric current density, A m^{-2}
B^{*} = External magnetic field, T

I. INTRODUCTION

Mixed convection in a cavity is an important phenomenon in many transport processes in nature and in engineering devices. Indeed, the combination of forced and natural convections has been recommended for high heat dissipating electronic components, where natural convection is notable for providing effective cooling. Significance of the mixed convection flow can be found in atmospheric flows, solar energy storage, heat exchangers, lubrication technology, drying technologies, and cooling the electronic devices. A brief review of literature shows that the study of mixed convection heat transfer in enclosures has attracted remarkable attention in the past few decades.[1–6]

Due to porous media dissipation area and its irregular motion of the fluid flow around the individual beads, using the porous media which can increase the heat transfer. On the other hand, the low conductivity of base fluids such as water has restricted designers. Fluids containing nano-sized solid particles offer a possible solution to conquer this problem. The nanofluid has greater effective thermal conductivity than based fluid. Nanofluids, a name conceived by Choi,[7] in Argonne National laboratory, are fluids consisting of solid nanoparticles with size less than 100 nm suspended with solid volume fraction typically less than 4%. Nanofluids can be used to improve thermal management system in many engineering applications such as transportation, micromechanics, instrument, and cooling devices.

A relatively few papers dealing with the mixed convection of nanofluids saturated in porous media were published; Ahmed and Pop[8] studied numerically the mixed convection of nanofluid past a vertical plate using three different nanoparticles based on the conventional model of Tiwari and Das[9] which incorporates only the nanofluid volume fraction. Cimpean and Pop[10] studied the fully developed steady-state mixed convection flow of nanofluids in an inclined porous channel. Hajipour and Dehkordi[11] considered mixed convection heat transfer of nanofluids based on the Brownian motion and thermophoresis in a vertical channel partially filled with highly porous medium using the Brinkman-Forchheimer model.

Matin and Ghanbari[12] studied the effects of Brownian motion and thermophoresis effect on the mixed convection of nanofluid in a porous channel including flow reversal. Recently, Srinivasacharya and Kumar[13] investigated mixed convection along an inclined wavy surface in a nanofluid saturated porous medium with wall heat flux. Conjugate heat transfer of MHD non-Darcy mixed convection flow of a nanofluid over a vertical slender hollow cylinder embedded in porous media is investigated by Jafarian *et al.*[14]

All the aforementioned studies are based on the first-law analyses. Recently, the second-law based investigations have gained attention for studying thermal systems. Entropy generation has been used as a gauge to evaluate the performance of thermal system. The analysis of the exergy utilization and the entropy generation has become one of the primary objectives in designing a thermal system. Bejan[15,16] focused on the different reasons behind entropy generation in applied thermal engineering. Generation of entropy destroys the available work of the system. Therefore it makes a good engineering sense of focus on the irreversibility of heat transfer and fluid friction process. There are only a very few studies that consider the second law analyzes in the presence of nanofluid as a working fluid in porous media. The effect of heat transfer in flow of nanofluids over a permeable stretching wall in a porous medium is investigated by Sheikholeslami *et al.*[17] They showed that an increase in the nanoparticle volume fraction decreases the momentum boundary layer thickness and entropy generation rate whereas the thermal boundary layer thickness increases. Ting *et al.*[18] studied the entropy generation of viscous dissipative nanofluid flow in thermal non-equilibrium porous media embedded in micro-channels. Ismael *et al.*[19] have studied the entropy generation due to conjugate natural convection conduction heat transfer in a square domain under steady-state condition. They proposed a new criterion for the assessment of the thermal performance. In some applications like fluoro-plastic coating (e.g., Teflon) which resist adhesion, the no-slip boundary condition imposed on the tangential velocity cannot be held. Moreover, some surfaces are rough or porous such that equivalent slip occurs.[20] A brief review of the literature[21–26] shows that due to practical importance, the study of heat transfer and fluid flow for various geometries with partial slip boundary conditions has attracted remarkable attention in the past few years. Recently, Alizadeh *et al.*[27] studied unaxisymmetric stagnation-point flow and heat transfer of a viscous fluid on a moving cylinder with time-dependent axial velocity. They also investigated MHD unaxisymmetric stagnation-point flow and heat transfer of a viscous fluid on a stationary cylinder[28] and unaxisymmetric stagnation-point flow and heat transfer of a viscous fluid with variable viscosity on a cylinder in constant heat flux.[29]

The literature survey above led us to be sure that the effects of the presence and locations and lengths of a heat sink and a heat source and entropy generation on the mixed convection of a nanofluid in porous media filled in a lid-driven square enclosure with partial slip and subjected to a magnetic field has not been investigated yet. Therefore, the purpose of this work is to carry out a comprehensive numerical study on this problem. It is believed that this study will contribute in improving the thermal performance in some engineering instruments.

II. PROBLEM DESCRIPTION AND MATHEMATICAL MODEL

The geometry of the present study, the steady two-dimensional mixed convection of nanofluid inside a square porous enclosure of length H filled with a nanofluid, is shown in Figure 1. The coordinates x and y are chosen such that x measures the distance along the bottom horizontal wall while y measures the distance along the left vertical wall, respectively. A heat source and a heat sink are located on a part of the bottom and upper walls, respectively, with length b. Two parts of the upper and bottom walls of the enclosure are maintained at T_c and T_h such that $T_h > T_c$ while the other parts are thermally insulated. The left and right walls are adiabatic and move at a constant and equal velocity V_0. A magnetic field with strength B_0 is applied at an angle Φ with the horizontal direction. The walls and the lid of the cavity are considered to be perfectly electrically conductive.

The nanofluids used in the analysis are assumed to be incompressible and laminar, and the base fluid (water) and the solid spherical nanoparticles (Cu) are in thermal equilibrium. The single phase approach is used for modeling the nanofluid heat transfer. The porous medium is also assumed with a very low electrical conductivity, i.e., electrically insulated porous medium. The thermo-physical properties of the base fluid and the nanoparticles are given in Table I. The thermo-physical properties of the nanofluid are assumed constant except for the density variation which is determined based on the Boussinesq approximation. Under the above assumptions, the conservation of mass, and in the case of mixed convection, and also the conservation of energy equations can be written as in Refs. 30–32,

$$\nabla \mathbf{u} = 0, \tag{1}$$

$$\frac{\rho_{nf}}{\varepsilon^2}\mathbf{u}\,.\,\nabla\mathbf{u} = -\nabla p - \frac{\mu_{nf}}{K}\mathbf{u} + \frac{\mu_{nf}}{\varepsilon}\nabla^2\mathbf{u} + \rho_{nf}\beta_{nf}(T - T_0)\mathbf{g} + \mathbf{J}\times\mathbf{B}^*, \tag{2}$$

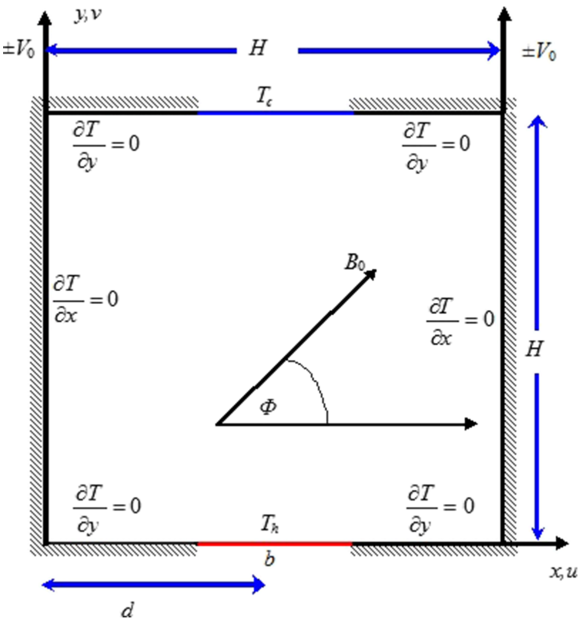

FIG. 1. Schematic diagram of the problem under consideration.

TABLE I. Thermo-physical properties of water and nanoparticles.[42]

Property	Water	Copper (Cu)
ρ	997.1	8933
C_p	4179	385
k	0.613	401
β	21×10^{-5}	1.67×10^{-5}
σ	0.05	5.96×10^{7}

$$\mathbf{u}\cdot\nabla T = \alpha_{eff,nf}\nabla^2 T + \frac{Q_0}{(\rho C_p)_{nf}}, \tag{3}$$

$$\nabla^2\Omega = \mathbf{B}^*\cdot\nabla\times\mathbf{u}, \tag{4}$$

$$\mathbf{J} = \sigma_{nf}\left(-\nabla\Omega + \mathbf{u}\times\mathbf{B}^*\right). \tag{5}$$

Here, u = (u, v) is the velocity vector, K is the permeability of the porous medium, **g** is the gravitational acceleration vector, μ_{nf} is the nanofluid dynamic viscosity, p is the pressure, $\boldsymbol{J}$ is the electric current, B^* is the external magnetic field, ρ_{nf} is the density of the nanofluid, Tis is the temperature of the nanofluid, T_0 is the average temperature $(T_c + T_h)/2$, Ω is the electric potential, σ_{nf} is the electrical conductivity, β_{nf} is the coefficient of thermal expansion of the nanofluid, and $(C_p)_{nf}$ is the heat capacitance of the nanofluid. Here, $\alpha_{eff\,,\,nf}$ is the effective thermal diffusivity of the nanofluid and the porous medium.

Sreenivasan *et al.*[33] have discussed the effect of magnetic field on the flow motion and concluded that for the case of a two-dimensional steady flow and where the magnetic field lies in the plane of motion, the term $\mathbf{B}^*\cdot\nabla\times\mathbf{u}$ is zero. Hence, Eq. (4) reduces to

$$\nabla^2\Omega = 0. \tag{6}$$

Taking into account that the enclosure walls are perfectly electrically conductive, they could provide a very low resistance guide path for the induced current. Therefore, it can be concluded that the electric field vanishes everywhere in the cavity.[34] Invoking these conditions, the term $\boldsymbol{J}\times\boldsymbol{B}^*$ in the momentum equation reduces to $\sigma_{nf}B_0^2u$.[35]

The governing equations can be expressed as follows:

$$\frac{\partial u}{\partial x} + \frac{\partial v}{\partial y} = 0, \tag{7}$$

$$\frac{1}{\varepsilon^2}\left(u\frac{\partial u}{\partial x} + v\frac{\partial u}{\partial y}\right) = -\frac{1}{\rho_{nf}}\frac{\partial p}{\partial x} + \frac{\upsilon_{nf}}{\varepsilon}\left(\frac{\partial^2 u}{\partial x^2} + \frac{\partial^2 u}{\partial y^2}\right) - \frac{\upsilon_{nf}}{K}u + \frac{\sigma_{nf}B_0^2}{\rho_{nf}}(v\,\sin\Phi\,\cos\Phi - u\,\sin^2\Phi), \tag{8}$$

$$\frac{1}{\varepsilon^2}\left(u\frac{\partial v}{\partial x} + v\frac{\partial v}{\partial y}\right) = -\frac{1}{\rho_{nf}}\frac{\partial p}{\partial y} + \frac{\upsilon_{nf}}{\varepsilon}\left(\frac{\partial^2 v}{\partial x^2} + \frac{\partial^2 v}{\partial y^2}\right) - \frac{\upsilon_{nf}}{K}v + \frac{\sigma_{nf}B_0^2}{\rho_{nf}}(v\,\sin\Phi\,\cos\Phi - u\,\sin^2\Phi) + \frac{(\rho\beta)_{nf}}{\rho_{nf}}g(T - T_0), \tag{9}$$

$$u\frac{\partial T}{\partial x}+v\frac{\partial T}{\partial y}=\alpha_{eff,nf}\left(\frac{\partial^2 T}{\partial x^2}+\frac{\partial^2 T}{\partial y^2}\right)+\frac{Q_0}{(\rho C_p)_{nf}}(T-T_0), \tag{10}$$

where u and v are the velocity components along the x-axis and y-axis, respectively, T is the fluid temperature, p is the fluid pressure, g is the gravity acceleration, Q_0 is the heat generation coefficient, ρ_{nf} is the density, μ_{nf} is the dynamic viscosity, ν_{nf} is the kinematic viscosity, and ε is the porous medium porosity. The effective thermal diffusivity of the nanofluid and the porous medium, $\alpha_{eff,nf}$, can be represented as $k_{eff,nf}/(\rho_{\mathrm{nf}}C_{nf})$, where $k_{eff,nf}$ is the effective thermal conductivity of the nanofluid and the porous medium; C_{nf} is the specific heat capacity of the nanofluid.

The boundary conditions are as follows:

$$\text{On the bottom wall:}\quad \begin{aligned} &y=0,\ u=v=0,\\ &T=T_h,\ (d-0.5b)\le x\le(d+0.5b),\\ &\frac{\partial T}{\partial y}=0\quad otherwise, \end{aligned} \tag{11a}$$

$$\text{On the top wall:}\quad \begin{aligned} &y=H,\ u=v=0,\\ &T=T_c,\ (d-0.5b)\le x\le(d+0.5b),\\ &\frac{\partial T}{\partial y}=0\ otherwise, \end{aligned} \tag{11b}$$

$$\text{On the right wall:}\quad \begin{aligned} &x=H,\quad u=\frac{\partial T}{\partial x}=0,\\ &v=\lambda_r V_0+N\mu_{nf}\frac{\partial v}{\partial x}, \end{aligned} \tag{12a}$$

$$\text{On the left wall:}\quad \begin{aligned} &x=0,\ u=\frac{\partial T}{\partial x}=0,\\ &v=\lambda_l V_0+N\mu_{nf}\frac{\partial v}{\partial x}. \end{aligned} \tag{12b}$$

A. Thermo-physical properties of nanofluid

The effective density of the nanofluid is given as[36]

$$\rho_{nf}=(1-\phi)\rho_f+\phi\rho_p, \tag{13}$$

where ϕ is the solid volume fraction of the nanofluid, ρ_f and ρ_p are the densities of the fluid and of the nanoparticles, respectively. The heat capacitance of the nanofluid is given by the following equation:[36]

$$(\rho c_p)_{nf}=(1-\phi)(\rho c_p)_f+\phi(\rho c_p)_p. \tag{14}$$

The thermal expansion coefficient of the nanofluid can be determined by the following equation:[37]

$$(\rho\beta)_{nf}=(1-\phi)(\rho\beta)_f+\phi(\rho\beta)_p, \tag{15}$$

where β_f and β_p are the coefficients of thermal expansion of the fluid and of the nanoparticles, respectively.

The thermal diffusivity, α_{nf}, of the nanofluid is defined by Abu-Nada and Chamkha[37] as

$$\alpha_{nf}=\frac{k_{nf}}{(\rho c_p)_{nf}}. \tag{16}$$

In Eq. (16), k_{nf} is the thermal conductivity of the nanofluid which for spherical nanoparticles, according to the Maxwell-Garnetts model[38] is given by

$$\frac{k_{nf}}{k_f}=\frac{(k_p+2k_f)-2\phi(k_f-k_p)}{(k_p+2k_f)+\phi(k_f-k_p)}. \tag{17a}$$

Following the study of Ghalambaz *et al.*,[39] the effective thermal conductivity of the porous medium and the nanofluid is evaluated using

$$k_{eff,\,nf}=\varepsilon k_{nf}+(1-\varepsilon)\,k_s, \tag{17b}$$

where k_s is the solid thermal conductivity and ε is the porosity of the porous medium. Accordingly, the effective thermal conductivity of the base fluid and the porous medium ($\mathrm{k_{eff,f}}$) can be evaluated using the following equation:

$$k_{eff,\,f}=\varepsilon k_f+(1-\varepsilon)\,k_s. \tag{17c}$$

These equations are valid when the thermal conductivity of the solid and the fluid is close as discussed in Ref. 40. Hence, in representing the results, the thermal conductivity of the fluid and the porous medium has been considered very close.

The effective thermal diffusivity of the nanofluid and the porous matrix is also introduced as follows:

$$\alpha_{eff,\,nf}=\frac{k_{eff,nf}}{\left(\rho c_p\right)_{nf}}. \tag{17d}$$

The effective dynamic viscosity of the nanofluid based on the Brinkman model[41] is given by

$$\mu_{nf}=\frac{\mu_f}{(1-\phi)^{2.5}}, \tag{18}$$

The effective electrical conductivity of the nanofluid is presented by Maxwell[38] as

$$\frac{\sigma_{nf}}{\sigma_f}=1+\frac{3(\gamma-1)\phi}{(\gamma+2)-(\gamma-1)\phi}, \tag{19}$$

where $\gamma=\frac{\sigma_p}{\sigma_f}$.

B. Dimensionless forms of equations

The following non-dimensional parameters are introduced:

$$\begin{gathered} X=\frac{x}{H},\ Y=\frac{y}{H},\ U=\frac{u}{V_0},\ P=\frac{p}{\rho_{nf}{V_0}^2},\ \theta=\frac{(T-T_0)}{\Delta T},\\ Ri=\frac{Gr}{\mathrm{Re}^2},\ S_l=S_r=\frac{N\mu_f}{H},\Delta T=(T_h-T_c),\ T_0=\frac{T_c+T_h}{2},\\ Q=\frac{Q_0H^2}{\left(\rho c_p\right)_f\alpha_f},B=\frac{b}{H},\ D=\frac{d}{H} \end{gathered} \tag{20}$$

into Eqs. (8)–(11) to yield the following dimensionless equations:

$$\frac{\partial U}{\partial X}+\frac{\partial V}{\partial Y}=0, \tag{21}$$

$$\frac{1}{\varepsilon^2}\left(U\frac{\partial U}{\partial X}+V\frac{\partial U}{\partial Y}\right)=-\frac{\partial P}{\partial X}+\frac{1}{\varepsilon\,\mathrm{Re}}\frac{\rho_f}{\rho_{nf}}\left(\frac{\mu_{nf}}{\mu_f}\right)\left(\frac{\partial^2 U}{\partial X^2}+\frac{\partial^2 U}{\partial Y^2}-\frac{\varepsilon U}{Da}\right)+\left(\frac{\rho_f}{\rho_{nf}}\right)\left(\frac{\sigma_{nf}}{\sigma_f}\right)\frac{Ha^2}{\mathrm{Re}}(V\sin\Phi\cos\Phi-U\sin^2\Phi), \tag{22}$$

$$\begin{aligned}\frac{1}{\varepsilon^2}\left(U\frac{\partial V}{\partial X}+V\frac{\partial V}{\partial Y}\right)=&-\frac{\partial P}{\partial Y}+\frac{1}{\varepsilon\,\mathrm{Re}}\frac{\rho_f}{\rho_{nf}}\left(\frac{\mu_{nf}}{\mu_f}\right)\left(\frac{\partial^2 V}{\partial X^2}+\frac{\partial^2 V}{\partial Y^2}-\frac{\varepsilon V}{Da}\right)+Ri\frac{(\rho\beta)_{nf}}{\rho_{nf}\beta_f}\theta\\&+\left(\frac{\rho_f}{\rho_{nf}}\right)\left(\frac{\sigma_{nf}}{\sigma_f}\right)\frac{Ha^2}{\mathrm{Re}}(U\sin\Phi\cos\Phi-V\cos^2\Phi),\end{aligned} \tag{23}$$

$$U\frac{\partial\theta}{\partial X}+V\frac{\partial\theta}{\partial Y}=\frac{1}{\mathrm{Pr}\,\mathrm{Re}}\frac{\alpha_{eff,nf}}{\alpha_{eff\,f}}\left(\frac{\partial^2\theta}{\partial X^2}+\frac{\partial^2\theta}{\partial Y^2}\right)+\frac{1}{\mathrm{Re}\,\mathrm{Pr}}\frac{(\rho\,c_p)_f}{(\rho\,c_p)_{nf}}Q\theta, \tag{24}$$

where

$$\mathrm{Pr}=\frac{\nu_f}{\alpha_{eff\,f}},\ \mathrm{Re}=\frac{V_0H}{\nu_f},\ Gr=\frac{g\beta_f H^3\Delta T}{\nu_f^2},\ Ri=\frac{Gr}{\mathrm{Re}^2},\ Ha=B_0H\sqrt{\sigma_f/\mu_f},\ Da=K/H^2,\ \alpha_{eff,nf}=\frac{k_{eff,nf}}{\left(\rho c_p\right)_{nf}},\ \alpha_{eff,f}=\frac{k_{eff,f}}{\left(\rho c_p\right)_f}.$$

The above parameters are the Prandtl number, Reynolds number, Grashof number, Richardson number, Hartmann number, and the Darcy number, respectively. In Eqs. (11) and (24), the heat generation due to viscous dissipation and Darcy dissipation and Joule heat generation due to the applied magnetic field is neglected. The viscous dissipation term is directly proportional to the Brinkman number defined as $Br=\frac{\mu V_0^2}{k\Delta T}=\mathrm{Pr}\,Ec$ with k and ΔT as the conductivity and the temperature difference, where $Ec=\frac{V_0^2}{(C_p)_f\Delta T}$ is the Eckert number. The Joule heat generation term and the Darcy dissipation are also directly proportional to $BrHa^2$ and $\frac{Br}{Da}$, respectively. The Brinkman number implies the ratio of the viscous dissipation to heat conduction. In the present study, the order of magnitude of the aforementioned terms is negligible in comparison with the other terms of the energy equation. (The order of the Brinkman number for the present study is approximately $10^{-6}(O(\frac{\mu V_0^2}{k\Delta T})\approx\frac{10^{-3}(10^{-2})^2}{0.1(1)}).)$

The dimensionless boundary conditions for Eq. (12) are written as follows:

$$\text{On the bottom wall:}\quad \begin{array}{l} Y=0,\ U=V=0,\\ \theta=0.5,\ (D-0.5B)\le X\le(D+0.5B),\\ \dfrac{\partial\theta}{\partial Y}=0\ \ otherwise,\end{array}$$

$$\text{On the top wall:}\quad \begin{array}{l} Y=1,\ U=V=0,\\ \theta=-0.5,\ (D-0.5B)\le X\le(D+0.5B),\\ \dfrac{\partial\theta}{\partial Y}=0\quad otherwise,\end{array}$$

$$\text{On the right wall:}\quad \begin{array}{l} X=1\ U=\dfrac{\partial\theta}{\partial X}=0,\\ V=\lambda_r+\dfrac{S_r}{(1-\phi)^{2.5}}\dfrac{\partial V}{\partial X},\end{array}$$

$$\text{On the left wall:}\quad \begin{array}{l} X=1,\ U=\dfrac{\partial\theta}{\partial X}=0,\\ V=\lambda_l+\dfrac{S_l}{(1-\phi)^{2.5}}\dfrac{\partial V}{\partial X}.\end{array} \tag{25}$$

The local Nusselt number is defined as

$$Nu_s=-\frac{k_{eff,nf}}{k_{eff\,f}}\left(\frac{\partial\theta}{\partial Y}\right)_{Y=0,1} \tag{26}$$

and the average Nusselt number is defined as

$$Nu_{m0}=\left(\frac{1}{B}\int_{D-0.5B}^{D+0.5B}Nu_s\,dX\right)_{Y=0},$$

$$Nu_{m1}=\left(\frac{1}{B}\int_{D-0.5B}^{D+0.5B}Nu_s\,dX\right)_{Y=1},$$

$$Nu_m=\frac{Nu_{m0}+Nu_{m1}}{2}. \tag{27}$$

C. Governing equation for entropy generation

The entropy generation in the flow field is caused by the non-equilibrium flow imposed by boundary conditions. According to Mahmud and Fraser,[43] the dimensional local entropy generation can be expressed by

$$\begin{aligned}s=&\left(\frac{k_{nf}}{T_0^2}\right)\left[\left(\frac{\partial T}{\partial x}\right)^2+\left(\frac{\partial T}{\partial y}\right)^2\right]+\left(\frac{\mu_{nf}}{T_0}\right)\left\{\frac{1}{K}(u^2+v^2)\right.\\&\left.+2\left[\left(\frac{\partial u}{\partial x}\right)^2+\left(\frac{\partial v}{\partial y}\right)^2\right]+\left(\frac{\partial u}{\partial y}+\frac{\partial v}{\partial x}\right)^2\right\}\\&+\left(\frac{\sigma_{nf}}{T_0}\right)B_0^2\,(u\,\sin\Phi-v\,\cos\Phi)^2.\end{aligned} \tag{28}$$

In Eq. (28), the first term represents the dimensional entropy generation due to heat transfer (s_h), the second term represents the dimensional entropy generation due to fluid fraction irreversibility resulting from Darcy dissipation and viscous dissipation (s_v), and the third term is the dimensional entropy generation due to the effect of the magnetic field (s_j). The entropy generation due to internal heat generation in the fluid and the porous media has been taken into account. Indeed, the internal heat generation results in a temperature gradient that can be seen in the calculations of the entropy generation.[44] It is worth noting that the internal heat generation can be assumed smooth and weak such as a porous collector for absorbing the solar energy or a matrix of porous media with very weak radioactive effects. By using the dimensionless parameters presented in Eq. (20), the expression of the non-dimensional entropy generation, (S), can be written as

$$
\begin{aligned}
S = s.\frac{H^2.T_0^2}{k_f(\Delta T)^2} &= \left(\frac{k_{eff,nf}}{k_{eff,f}}\right)\left[\left(\frac{\partial\theta}{\partial X}\right)^2+\left(\frac{\partial\theta}{\partial Y}\right)^2\right] \\
&+ \Theta.\left(\frac{\mu_{nf}}{\mu_f}\right).\mathrm{Re}^2.\mathrm{Pr}^2\left\{\frac{1}{Da}(U^2+V^2)+2\left[\left(\frac{\partial U}{\partial X}\right)^2+\left(\frac{\partial V}{\partial Y}\right)^2\right]+\left(\frac{\partial V}{\partial X}+\frac{\partial U}{\partial Y}\right)^2\right\} \\
&+ \Theta.\left(\frac{\sigma_{nf}}{\sigma_f}\right).Ha^2.\mathrm{Re}^2.\mathrm{Pr}^2.(U\sin\Phi - V\cos\Phi)^2 = S_h + S_v + S_j,
\end{aligned}
\tag{29}
$$

where $\mathrm{S_h}$, $\mathrm{S_v}$, and $\mathrm{S_j}$ are the dimensionless local entropy generation rate due to heat transfer, the fluid fraction, and the Joule heating, respectively. In Eq. (29), Θ is the irreversibility factor which represents the ratio of the viscous entropy generation to thermal entropy generation. It is given as

$$\Theta = \frac{\mu_f.T_0}{k_f}\left(\frac{\alpha_{eff,f}}{\Delta T\, H}\right)^2. \tag{30}$$

The Bejan number, Be, defined as the ratio between the entropy generation due to heat transfer by the total entropy generation, is expressed as

$$Be = \frac{Sh}{S}. \tag{31}$$

In order to present the effect of nanoparticles, magnetic field and the difference of temperature on the average Nusselt number, total entropy generation, and the Bejan number, the following Nusselt number ratio, total entropy generation ratio, and Bejan number ratio are defined,

$$Nu^+ = \frac{Nu_m}{(Nu_m)_{\phi=0}} \quad \text{and} \quad Nu^{++} = \frac{Nu_m}{(Nu_m)_{Ha=0}}, \tag{32}$$

$$S^+ = \frac{S}{(S)_{\phi=0}} \quad \text{and} \quad S^{++} = \frac{S}{(S)_{Ha=0}}, \tag{33}$$

$$Be^+ = \frac{Be}{(Be)_{\phi=0}} \quad \text{and} \quad Be^{++} = \frac{Be}{(Be)_{Ha=0}}. \tag{34}$$

III. NUMERICAL SOLUTION AND VALIDATION

In the present study, the finite volume method is used to solve the governing equations. This method integrates the governing equations over finite control volumes and results in a set of algebraic equations that can be solved numerically. Staggered grids have been used where the velocity components are calculated at the center of the volume interfaces while the pressure as well as other scalar quantities such as the temperature is computed at the center of the control volumes. The algebraic discretization equations have been solved iteratively throughout the physical domain by using the well-known tridiagonal matrix algorithm (TDMA) technique. Pressure and velocity were coupled using the Semi Implicit Method for Pressure Linked Equations (SIMPLE).[45] Convergence of the iterative solution was ensured when the residual of all variables was less than 10^{-6}. The non-uniform grids were used in the computational domains. It consists of 101 × 101 grid nodes in the *x*- and *y*-directions, respectively. The obtained results are independent of the number of the grids. The grid independency results are given at $k_f = k_s$, $\varepsilon = 0.5$, $Ha = 10$, $Da = 10^{-3}$, $Pr = 6.2$, $Gr = Re = 10^4$, $D = 0.5$, $B = 0.5$, $Q = 1.0$, $\Phi = 45$, $\phi = 0.05$, $S_l = S_r = 1.0$, $\lambda_l = -\lambda_r = 1.0$ and presented in Table II.

Considering the heat transfer in porous media, Iwatsu *et al.*[30] have studied the mixed convection heat transfer in a lid-driven enclosure filled with a fluid-saturated porous medium in the presence of internal heat generation. Following Iwatsu *et al.*,[30] Khanafer and Chamkha[31] revisited the same problem by considering internal heat generation effects. In the studies of Iwatsu *et al.*[30] and Khanafer and Chamkha,[31] a square cavity was investigated in which the vertical side walls were assumed well insulated and the entire top wall was hot and the bottom wall was cold. The top lid was driven with a constant velocity. Neglecting the effect of the magnetic field and internal heat generation and by adopting the same boundary conditions as in the mentioned references, the present study and its governing equations can be reduced to the study of Iwatsu *et al.*[30] and Khanafer and Chamkha.[31] Considering $Re = 1000$, $Pr = 0.71$, $Gr = 100$, and $\phi = Ha = B = 1$, a comparison between the temperature contours of the present study and those reported in Iwatsu *et al.*[30] and Khanafer and Chamkha[31] is depicted in Fig. 2. The increment between each temperature contours is 0.05. The result shows a very good agreement between this work and the previously published work.

TABLE II. Grid-independency study for Cu-water nanofluid.

Grid-size	41 × 41	61 × 61	81 × 81	91 × 91	101 × 101	121 × 121
Nu_m	1.469 836	1.448 858	1.437 232	1.429 925	1.424 576	1.424 554

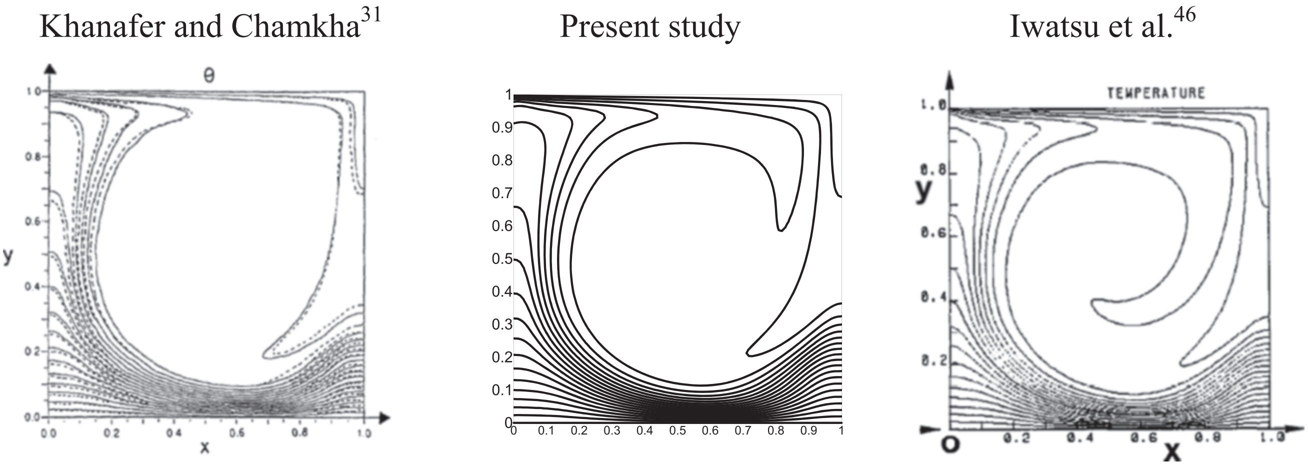

Khanafer and Chamkha[31]

Present study

Iwatsu et al.[46]

FIG. 2. Comparison of the present study with $Re = 1000$, $Pr = 0.71$, $Gr = 10^2$, $\phi = Ha = B = 0$.

Fig. 2 displays a comparison between the temperature contours presented in this work with those of Khanafer and Chamkha[31] and Iwatsu *et al.*[30] The result shows a very good agreement between this work and the previously published work.

Considering heat transfer in nanofluids, Abu-Nada and Chamkha[46] have studied the natural convective heat transfer of nanofluids in a lid driven cavity. The side walls of the cavity were insulated while the top and bottom walls were isothermal with a temperature difference and the hot wall was the driven lid. Considering the boundary conditions and the notation of Abu-Nada and Chamkha[46] and also neglecting the magnetic field effect, a comparison between the evaluated Nusselt numbers in the present study and those reported by Abu-Nada and Chamkha[46] is reported in Table III. The results of this table are reported for nanofluids with water as the base fluid and Al_2O_3 nanoparticles. As seen, a very good agreement between the results of both studies can be seen.

Considering the MHD effects, Sheikholeslami *et al.*[47] have addressed the free convection of Cu water nanofluids in a square enclosure. In the study of Sheikholeslami *et al.*,[47] the top wall of the cavity was well insulated while the vertical side walls were at a constant temperature Tc. The bottom wall was partially heated which was at a constant temperature Th. Following the boundary condition and notation of Sheikholeslami *et al.*,[47] the Nusselt number was reported as 9.429 when $Ra = 10^5$, $\varepsilon = 0.8$ (the bottom flash element length), $\phi = 0{:}04$, and $Ha = 100$. Here, we obtained the Nusselt number as 9.4286 which shows a very good agreement with the literature value.

TABLE III. A comparison between the results of the average Nusselt number in the present study and those reported by Abu-Nada and Chamkha[46] when $Ri = 0.2$, $Ha = 0$, $Gr = 100$, $Da \to \infty$ $B = Q = 0$.

ϕ	Abu-Nada and Chamkha[46]	Present study
10%	3.099	3.0976
7	2.958	2.9457
5	2.867	2.8541
2	2.732	2.7317
0	2.644	2.6441

IV. RESULTS AND DISCUSSION

Selective results represented by streamlines, isotherms, local and global entropy generation, local and global Bejan number, and local average Nusselt number are illustrated in this section. The effects of the heat sink and source length (B = 0.2-1) and location (D = 0.3-0.8) are discovered and discussed. The effects of each mentioned parameters are studied for various nanofluid volume fractions (ϕ = 0-0.1) and Hartmann numbers (Ha = 0-20). The order value of porosity is between 0 and 1 and the order of the Darcy number is related to the permeability (the order of K is less than 10^{-6} for many of materials) and size of cavity and some papers such as Kuznetsov[48] assumed that between 10^{-1} and 10^{-4}. Therefore, the results are obtained for the fixed parameters: Pr = 6.2, ε = 0.5, Da = 10^{-3}, Φ = 45°. As shown in Eq. (30), Θ is related to the fluid thermo-physical properties, size of the cavity and the sink, and source temperatures. Therefore, for a small size cavity and low difference between the sink and source temperatures, the fixed Θ can be assumed as 10^{-2}.

Three orders of thermal conductivity of the porous medium (k_s) are considered. These cases are as follows: (I) The thermal conductivity of the porous medium (k_s) and the base fluid (k_f) are the same $k_f = k_s$, (II) the thermal conductivity of the porous medium is higher than the thermal conductivity of the base fluid ($k_f = 0.5k_s$), and (III) the thermal conductivity of the porous medium is lower than the thermal conductivity of the base fluid ($k_f = 2k_s$). The porous medium is also assumed to have a very low electrical conductivity, i.e., electrically insulated porous medium.

So, in these cases and with focusing on the properties' relations, the order of Prandtl number Pr is near that of the fluid (for water Pr ≈ 6).

A. Effects of the heat sink and source length

Fig. 3 shows the effects of the heat sink and source length (B) on the streamlines, isotherms, local entropy generation, and the Bejan number for $Ri = 1(Gr = 10^4, Re = 10^2)$, $\phi = 0.05$, $Ha = 10$, $D = 0.5$, $\lambda_l = -\lambda_r = 1$, $S_l = S_r = 1$, $Q = 1$.

Generally, the effects of the buoyancy together with the imposed boundary conditions make the fluid rotate clockwise

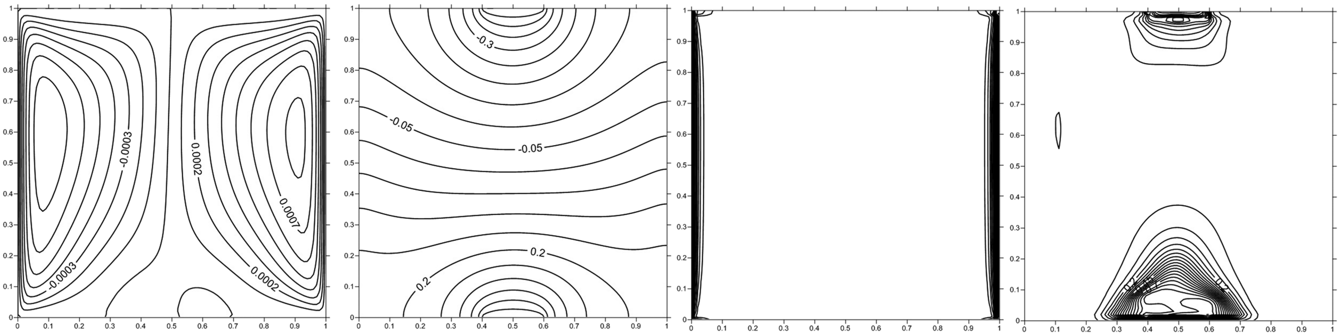

a) B=0.2

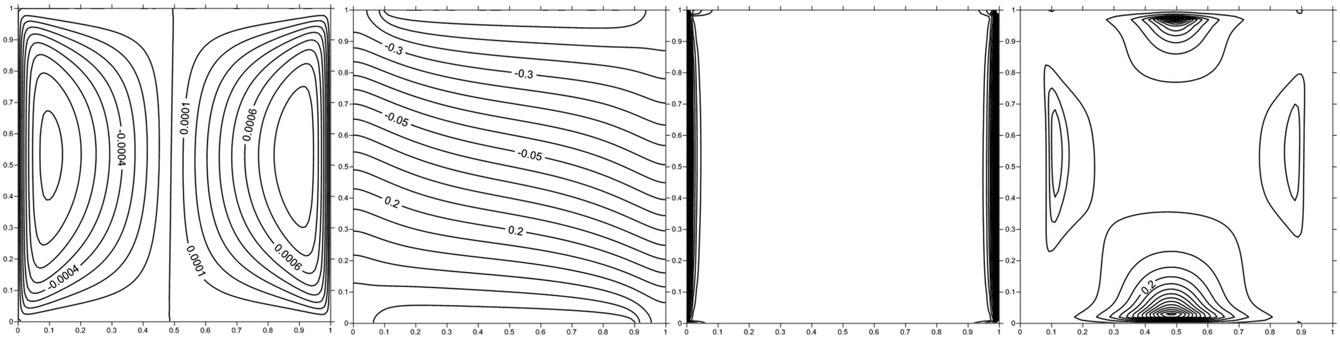

b) B=0.8

FIG. 3. Streamlines, isotherms, local entropy generation, and the local Bejan number for $\lambda_l = 1,\ \lambda_r = -1$.

with a single-cell circulation near the left wall and counterclockwise in the middle and near the right wall. The streamlines and the core shape of the cell are more symmetric when B is increased from 0.2 to 0.8. The isotherms tend to be horizontal in the middle of the cavity. The temperature gradient is significant near the source and is decreased through increasing B. The heat transfer irreversibility as well as the fluid friction irreversibility near the slip walls causes the entropy generation to experience a significant value near the left and the right walls. The entropy generation does not have a sensible value at the middle of the cavity but the heat transfer irreversibility is a dominant term in the entropy generation and therefore, the local Bejan number is visible at the middle of the cavity. With increasing values of B, the heat transfer irreversibility is enhanced, and thus, the local Bejan number shows more concentration in the middle of the cavity for B = 0.8.

Fig. 4 is presented for the same purpose and parameters of Fig. 3, but for $\lambda l = -\lambda r = 1$. On the contrary, with $\lambda l = \lambda r = 1$, the fluid rotates clockwise forming a single-cell circulation near the walls and at the center of cavity and converts to two weak vortices. The trend of these results is in agreement with the results of the study of Tiwari and Das.[9] The core shape of this cell is transformed from mostly vertically extended to mostly horizontally extended when B increases from 0.2 to 0.8. The isotherms tend to be vertical in the middle of the cavity when B = 0.2. The isotherm lines for the heat sink are more crowded than the heat source for both B = 0.2 and B = 0.8. The local entropy generation shows a similar trend to Fig. 2, but the local Bejan number is significant in the middle of the cavity and it vanishes near the heat source and sink because of the decrease in the temperature gradient for B = 0.8.

Fig. 5 illustrates the local Nusselt number (Nu_s) for both $\lambda_l = -\lambda_r = 1$ and $\lambda_l = \lambda_r = 1$. Fig. 5(a) illustrates Nu_s for $\lambda_l = -\lambda_r = 1$ at Y = 0. As shown in the isotherm lines in Fig. 3, the temperature gradient near the heat source is decreased by increasing B, thus, B = 0.2 shows the maximum value for Nu_s. The temperature gradient in the left side of the heat source is greater than that of the right side and the maximum value of Nu_s is, therefore, experienced at the beginning of the heat source for all ranges of B. The unsymmetrical temperature gradient is due to the motion of the lids. When the lids move in the same direction, two smooth circular cells can be seen in Fig. 3 (the case of streamlines). However, in the core regions, the induced flows tend to oppose each other and very low velocities (as seen in streamlines of Fig. 4) are observed. Thus, as a result, a uniform temperature distribution over the elements can be observed. In contrast, when the lids move in the opposite direction, a big circulation flow can be observed. Hence, following the induced big circulation cell, the parts of the elements, which are in aid with the circulation flow experience higher temperature gradients due to aiding of the fluid flow. By paying attention to the temperature contours of Fig. 4(a), it can obviously be seen that the temperature gradient at the right side of the bottom hot element is higher than that of the left side (the temperature contours are more close to each other). Indeed, this is due to the fact that the movement of the right lid toward the top tends to move the cooled fluid from the top cold element toward the hot element at the bottom. The same is true for the cold element at the top, in which, the left lid wall takes the warm fluid from the bottom and delivers it to the left side of the cold element. Therefore, according to the temperature distributions, a symmetric distribution of the Nusselt

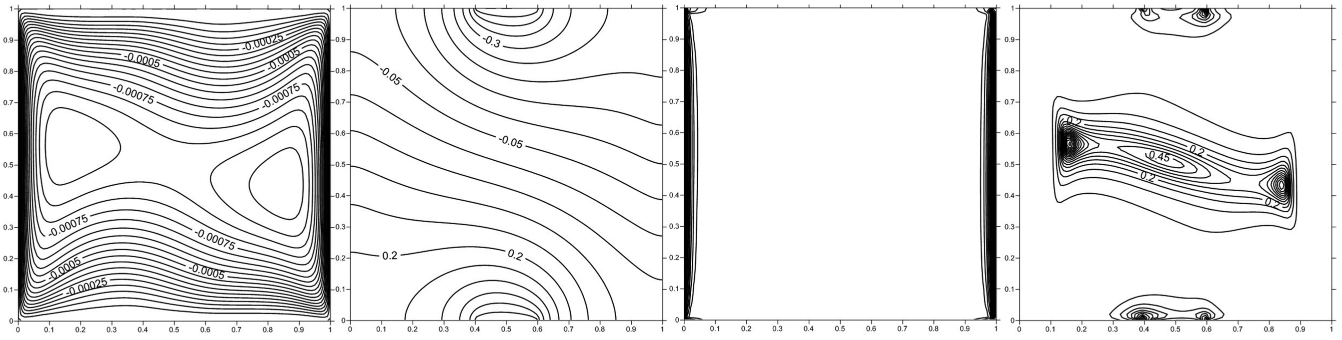

a) B=0.2

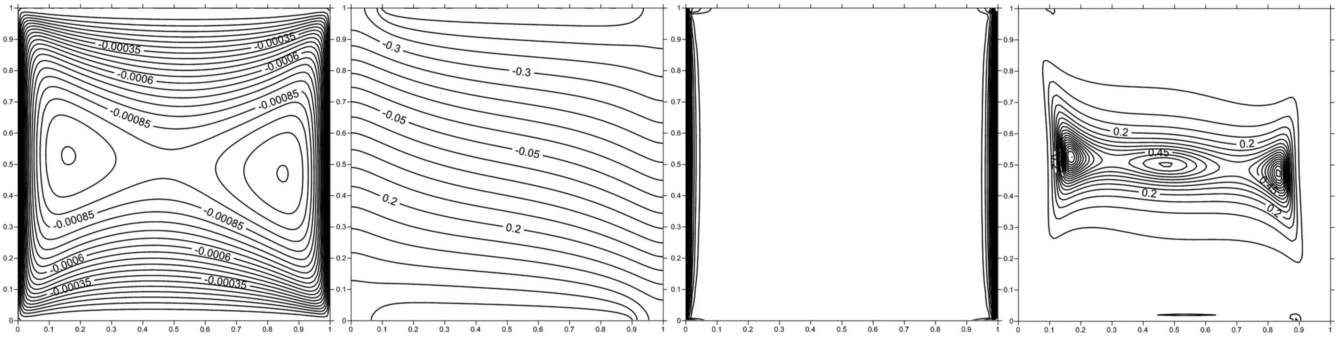

b) B=0.8

FIG. 4. Streamlines, isotherms, local entropy generation, and the local Bejan number for $\lambda_l = 1$, $\lambda_r = -1$.

number for Figs. 5(a) and 5(b) and an unsymmetrical one for Figs. 5(c) and 5(d) can be expected. The Nusselt numbers next to the edges of the elements are high which is due to the fact that these parts are the first parts that receive fresh fluids. For B = 0.8, $\mathrm{Nu_s}$ is almost equivalent on both sides of the source. The local Nusselt number is increased till the middle of B and then it is decreased with an axisymmetric trend for a fully heated bottom wall (B = 1). The scenario of decreasing $\mathrm{Nu_s}$ by increasing B is also obtained in Fig. 5(b), but the opposite trend is seen for $\mathrm{Nu_s}$ for each B; in other words, the maximum value of $\mathrm{Nu_s}$ occurs at the end of the sink. For a fully cooled top wall (B = 1), the beginning and the end of the heat sink experience equal maximum Nusselt numbers and minimum Nusselt numbers are seen at B = 0.5. Fig. 5(c) illustrates $\mathrm{Nu_s}$ for $\lambda_l = \lambda_r = 1$ at Y = 0. The isothermal lines in Fig. 4 indicate that the temperature gradient has a significant value at the end of the heat source, and hence, the maximum Nusselt number occurs at the end of it. The Nusselt number increases when B is increased because of the consequent increase in the temperature gradient. For B = 1, a continuous increment is observed for the local Nusselt number from the beginning to the end of the heat source. Fig. 5(d) shows that the maximum Nusselt number occurs at the beginning of heat sink for all values in the range of B. Also, the Nusselt number has a significant value at the end of heat sink. For B = 1, a continuous decrease is observed for the local Nusselt number from the beginning to the end of the heat sink.

Fig. 6 displays the variation of the average Nusselt number with the nanofluid volume fraction. Fig. 6(a) shows that the average Nusselt number decreases as the nanofluid volume fraction increases for all of the covered ranges of B at $k_f = k_s$ and $\lambda_l = -\lambda_r = 1$. Fig. 6(b) indicates that the Nu_m^+ decreases when the nanofluid volume fraction is increased. This scenario is seen for Figs. 6(c) and 6(d). As shown in Fig. 5, for $\lambda_l = \lambda_r = 1$, the integration of the local Nusselt number on the heat sink and source domains for all values of B is greater than that for $\lambda_l = -\lambda_r = 1$, and therefore, the average Nusselt number is relatively higher in the case of Fig. 6(a) compared to Fig. 6(c).

Ho *et al.*[49] have discussed the effect of utilizing different dynamic viscosity models for the analysis of the natural convection heat transfer of nanofluids in a cavity. Ho *et al.*[49] addressed the effect of utilizing Brinkman's model[40] as well as the relationship of Maïga *et al.*[50] for the dynamic viscosity of Al_2O_3-water nanofluids. Considering the Maxwell model for the thermal conductivity of the nanofluid, the following results were reported. Enhancement of heat transfer can be observed by utilizing Brinkman's model for the dynamic viscosity of Al_2O_3-water nanofluid. However, utilizing the relationship of Maïga *et al.*,[50] the results indicate a deterioration of heat transfer for high values of the Rayleigh number, i.e., convective dominant heat transfer regimes. In addition, in another study, Abu-Nada and Chamkha[37] also consider a logarithmic relation for the dynamic viscosity of CuO-EG-water nanofluid and studied the natural convection heat transfer in a cavity. The results reveal different trends of heat transfer enhancement or deterioration in a cavity due to the presence of nanoparticles. The observed trends of the behavior were mainly a function of the Rayleigh number. Indeed, both of the studies of Ho *et al.*[49] and Abu-Nada and Chamkha[37]

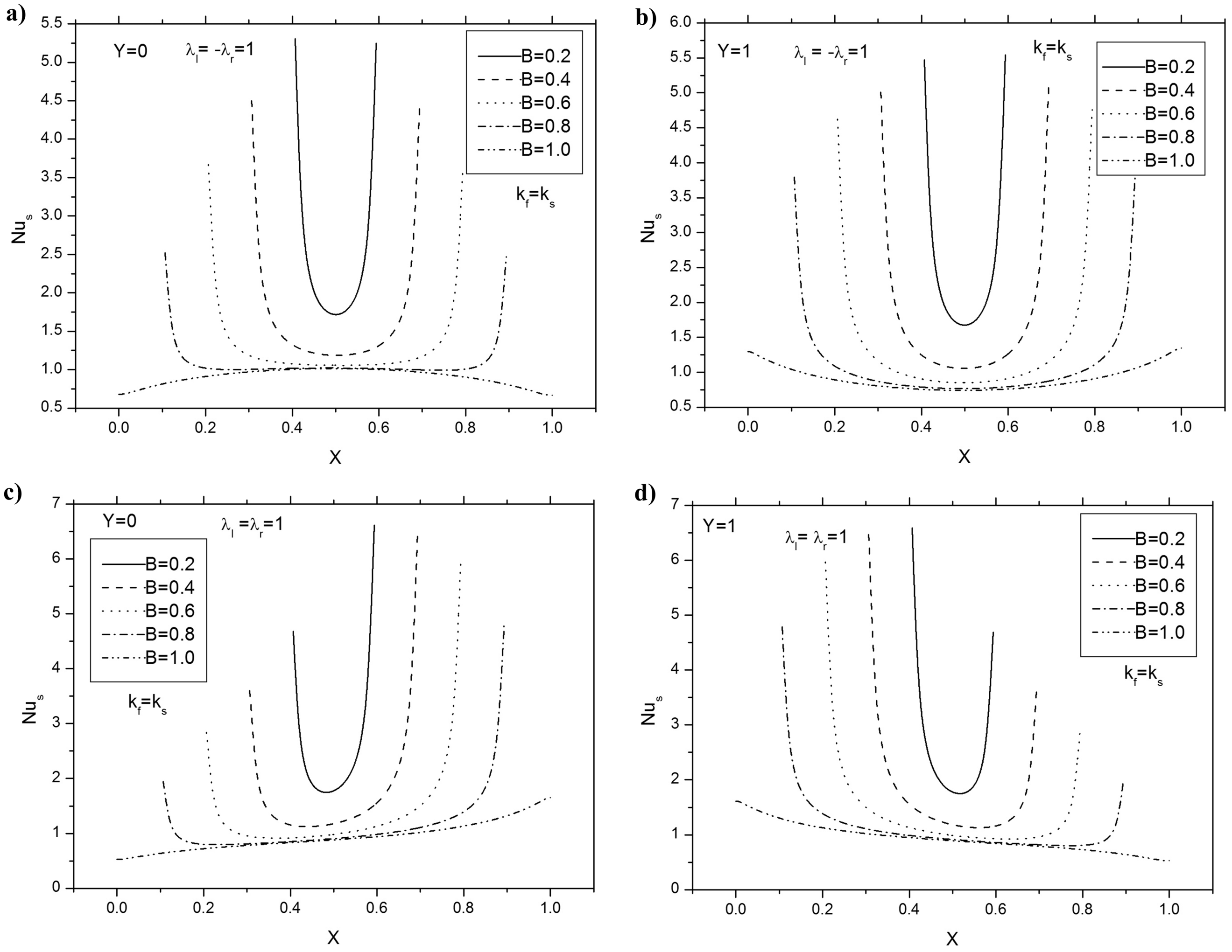

FIG. 5. Local Nusselt number for Cu-water for ((a) and (b)) $\lambda_l = \lambda_r = 1$ and ((c) and (d)) $\lambda_l = 1, \lambda_r = -1$.

reveal that the dynamic viscosity and the Rayleigh number are two important factors for the heat transfer behavior of nanofluids.

It is clear that the presence of nanoparticles would enhance the thermal conductivity of the synthesized nanofluid. Therefore, in the case of a quiescent fluid or a fluid with a very low velocity, for which the dominant mechanism of heat transfer is the conduction heat transfer mechanism, the presence of nanoparticles would enhance the heat transfer rate; no matter what the viscosity of the nanofluid is. However, as the Rayleigh number increases, the buoyancy forces get stronger and the fluid tends to move faster in the cavity. Consequently, the increase of the fluid motion boosts the role of the dynamic viscosity. It is clear that the increase of the dynamic viscosity due to the presence of the nanoparticles tends to induce more resistance due to shear forces against the fluid motion and decrease the fluid velocities. In fact, any reduction in the fluid velocities would directly reduce the heat transfer by the reduction of the advection mechanism. The reduction of the adjective heat transfer mechanism finally results in the decrease of the overall heat transfer in the cavity. When the deterioration in the heat transfer due to the increase of the viscosity overcomes the heat transfer enhancement due to the increase of the thermal conductivity due to the presence of nanoparticles, the reduction in the overall heat transfer can be expected. The analysis of viscosity models in the previous studies indicates that the Brinkman model almost predicts the lowest increase of the viscosity for nanofluids. Therefore, using the Brinkman model shifts the reduction of heat transfer toward the high values of the Rayleigh number or the flows beyond the laminar convection regime.

In the case of natural convection in a porous medium, the role of the dynamic viscosity is more effective compared to a regular fluid. This is due to the fact that in a regular clear space, the interaction of the fluid and the solid boundaries, which results in high gradient velocity regions next to the walls, is limited to the solid wall boundaries. However, in a porous space, the interaction between the solid structure of the porous matrix and the nanofluid is within the entire porous space as well as the wall boundaries. Therefore, in the natural or mixed convection heat transfer mechanism, occurring in the porous spaces, the reduction of heat transfer for smaller values of the Rayleigh number can be expected. The results of the very recent studies regarding the analysis of the natural convection of nanofluids in a cavity filled with a porous medium, for instance, the study of Ghalambaz *et al.*,[39] also confirm the reduction of heat transfer in natural convection in porous media. Ghalambaz *et al.*[39] have utilized the Brinkman

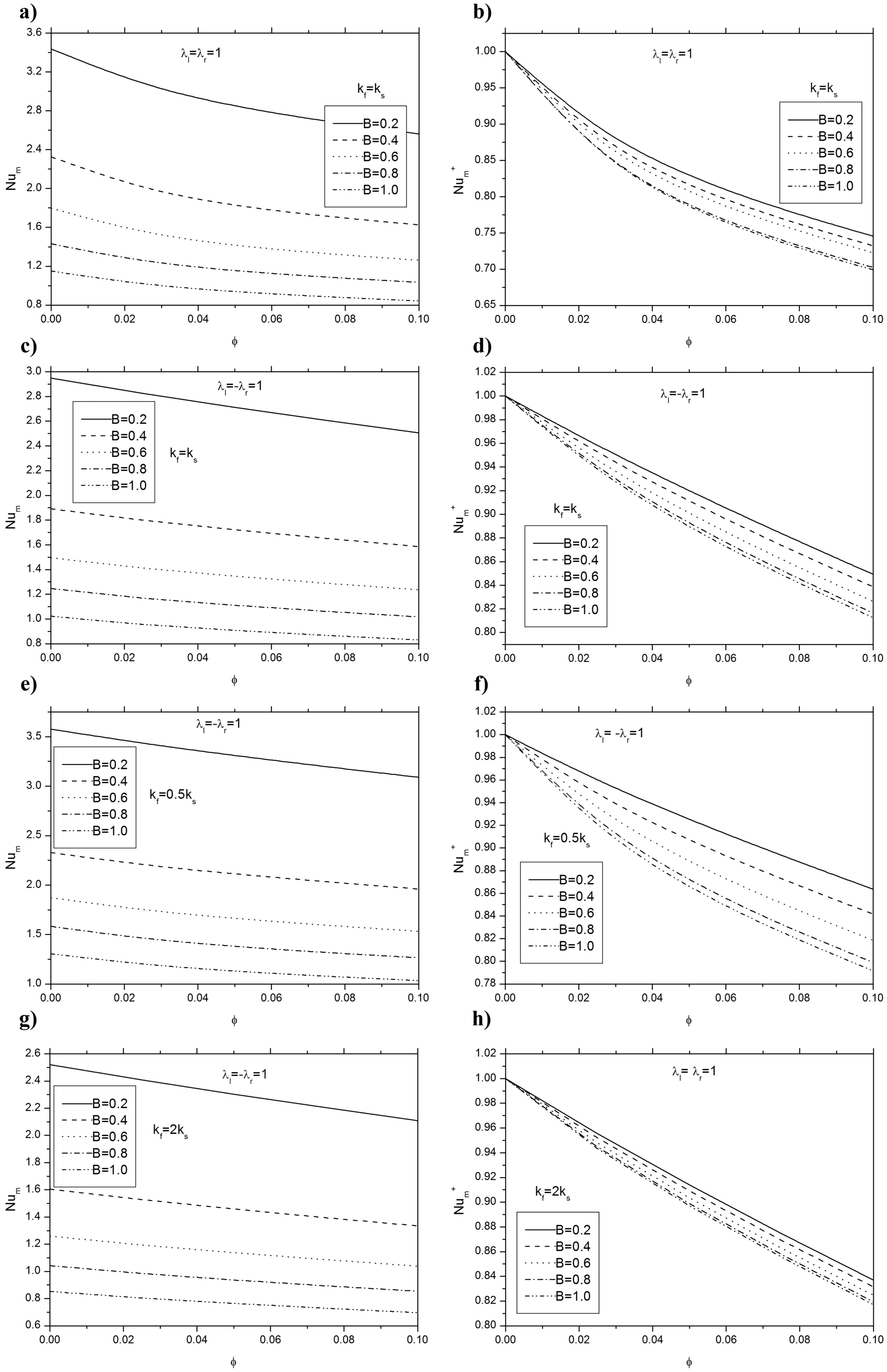

FIG. 6. Variation of the average Nusselt number of Cu-water with ϕ.

model for the dynamic viscosity and the Maxwell model for the thermal conductivity and reported the reduction of heat transfer due to the natural convection of nanofluids in a square cavity differentially heated from side walls.

Therefore, it can be concluded that adding very high conductive solid nanoparticles will generate a nanofluid with higher viscosity, higher density, and higher thermal conductivity. The first two properties increase the viscous and inertial forces, respectively, while the enhanced thermal conductivity increases the transferred thermal energy. Hence, the trend of the Nusselt number ratio presented in Fig. 6 elucidates that the enhanced viscous and inertial forces are dominant over the enhanced thermal conductivity and both buoyancy and shear effects in addition. Also, increasing the nanofluid volume fraction leads to increasing the viscosity and by increasing the viscosity of the nanofluid velocity is decreased and then the heat transfer is decreased as well. Figs. 6(e) and 6(f) show the continuous reduction of $\mathrm{Nu_m}$ and $\mathrm{Nu_m}$ ratio with increasing values of the nanofluid volume fraction for $k_f = 0.5k_s$ and $\lambda_l = -\lambda_r = 1$. For $k_f = 2k_s$, a similar trend can be seen in Figs. 6(g) and 6(h). Fig. 6 also shows that the fully heated bottom wall and the fully cooled top wall experience minimum Nusselt numbers compared with the other range of B. Also, for B = 0.2, the maximum Nusselt number is observed for all presented cases in Fig. 6.

Fig. 7 shows the variation of S^+ with the nanofluid volume fraction for both of $\lambda_l = -\lambda_r = 1$ (for $k_f = k_s$, $k_f = 0.5k_s$, and $k_f = 2k_s$) and $\lambda_l = \lambda_r = 1$ (for $k_f = k_s$). Figs. 7(a) and 7(d) show an increment in S^+ by increasing the nanofluid volume fraction but Figs. 7(b) and 7(c) show that S^+ decreases as a result of increasing ϕ at low nanofluid volume fractions and then increases with increasing values of ϕ for all covered ranges of B at $\lambda_l = \lambda_r = 1$ and $k_f = k_s$ and B = 0.6-1 at $\lambda_l = -\lambda_r = 1$ and $k_f = 0.5k_s$. As shown in Fig. 6, the Nusselt number decreasing rate for small values of the nanofluid volume fraction is more than that corresponding to higher values. This trend is because of the more decrease in temperature gradient, and so, the entropy generation because of the heat transfer irreversibility for low volume fractions is higher than that for higher values, leading to decreases in the values of S^+. For high volume fractions, the fluid friction irreversibility and the heat transfer irreversibility and Joule heat irreversibility lead to increasing S^+. Also, the figure shows that the entropy generation ratio is less than unity in the two mentioned cases for low nanofluid volume fractions. The different behaviors of Figs. 7(a) and 7(b) also may be because of the nanofluid velocity boundary between the two cases $\lambda_l = -\lambda_r = 1$ and $\lambda_l = \lambda_r = 1$ observed in the streamlines in Fig. 4 and its difference leads to a different behavior for fluid fraction irreversibility (FFI) and a different trend between Figs. 7(a) and 7(b). The different values of the effective conductivity of the porous media and heat transfer irreversibility (HTI) lead to higher value of S^+ in Fig. 7(d) compared Fig. 7(c).

Fig. 8 indicates the effect of the addition of nanoparticles to the pure fluid on Be^+. As shown in Fig. 8, Be^+ increases when ϕ is increased for all values of B and k_s for $\lambda_l = -\lambda_r = 1$ and $\lambda_l = \lambda_r = 1$. As shown in Fig. 7, the total entropy generation ratio, and because of the different velocity boundary manner between the two mentioned cases in Figs. 8(a) and 8(b), leads to different behaviors in the Bejan number ratio. The effective conductivity of the porous media is the main parameter for enhancing the HTI shown in Figs. 8(c) and 8(d).

Figs. 9–11 display the effect of the Hartmann number on the Nusselt number, total entropy generation, and the total

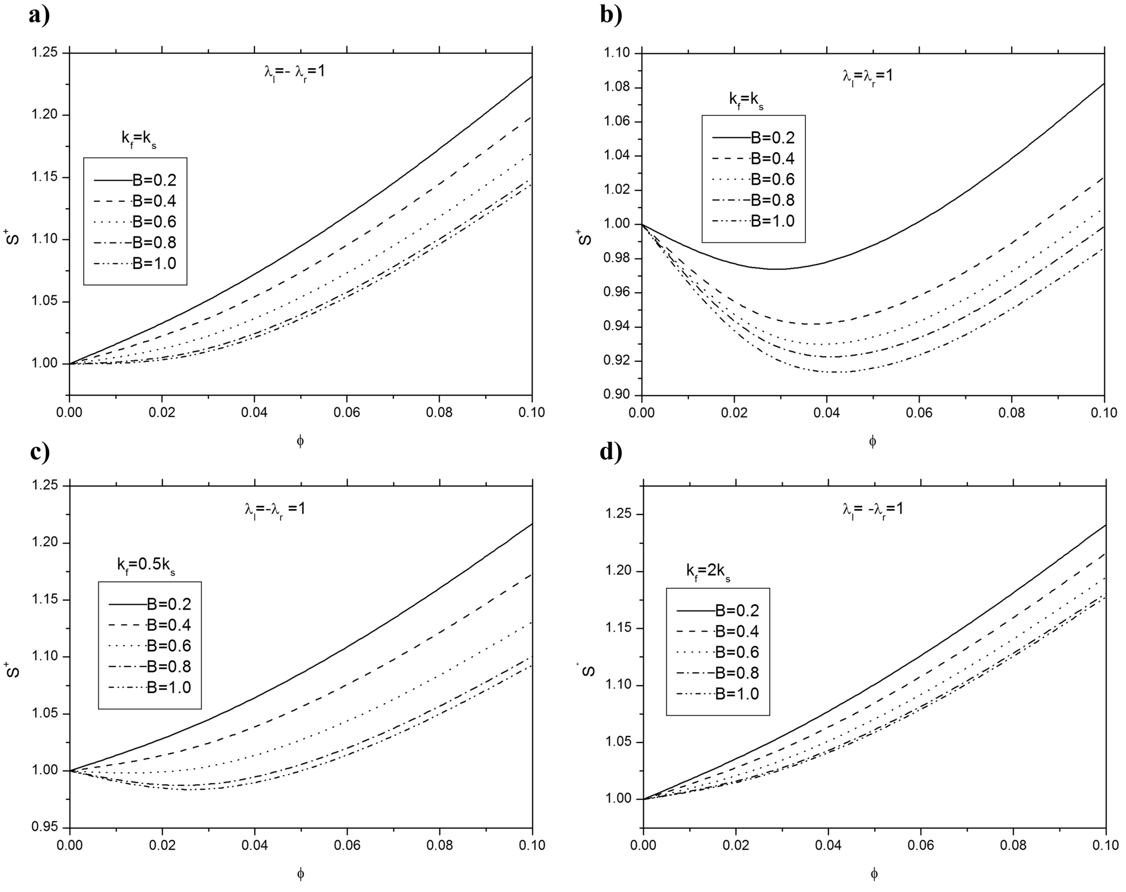

FIG. 7. Variation of the total entropy generation ratio with ϕ.

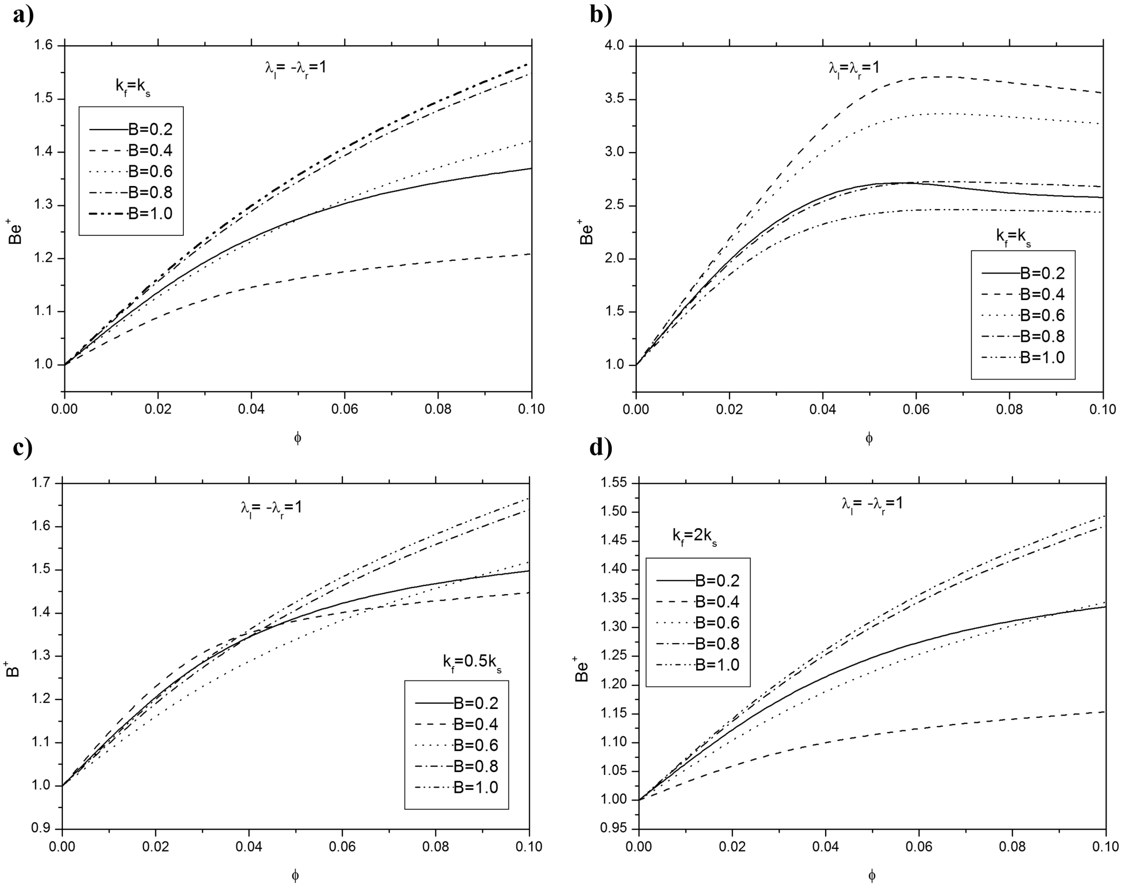

FIG. 8. Variation of the total Bejan number ratio with ϕ.

Bejan number for $Ri = 1$, $\phi = 0.05$, $D = 0.5$, $Sr = S_l = 1$, $Q = 1$. Fig. 9 illustrates the variation of the Nusselt number with respect to the Hartmann number (Ha). The results show that the Nusselt number decreases when the Hartmann number is increased for all ranges of B. As shown in Figs. 9(a) and 9(c), the reduction of the Nusselt number by increasing the Hartmann number is not very sensible, and therefore, the effect of the Hartmann number on Nu^{++} is investigated too and the effect of enhancement of Ha on Nu_m^{++} is presented in Figs. 9(b) and 9(d). This shows that the decreasing rate is much more when Ha > 10. In general, an external magnetic field leads to the suppression of the flow field, and therefore, the average Nusselt number is expected to decrease with the Hartmann number.

Fig. 10 depicts the effect of Ha on Be^{++}. Generally, Be^{++} increases with increasing values of Ha for B = 0.2-1 and $\lambda_l = \lambda_r = 1$, but for B = 0.2, Be^{++} shows a different behavior with the other curves. Fig. 10(a) shows that Be^{++} increases when Ha is increased for all ranges of B. The Lorentz force as well as the velocity boundary leads to a different trend of the Bejan number ratio with the Hartmann number.

The variation of S^{++} with Ha is presented in Fig. 11. As explained before, a very small decrease in the heat transfer irreversibility and, on the other hand, an increase in the Joule heat irreversibility because of increasing the value of Ha lead to a continuous increment in S^{++} as the value of Ha is increased for all ranges of B with $\lambda_l = -\lambda_r = 1$ and $\lambda_l = \lambda_r = 1$.

B. Effects of the heat sink and source location

The effects of the heat sink and source location are studied for $Ri = 1$, $Ha = 10$, $B = 0.5$, $S_r = S_l = 1$, $Q = 1$, and $k_s = k_f$. The streamlines, isotherms, total entropy generation, and the Bejan number for $\phi = 0.05$, $\lambda_l = 1$, $\lambda_r = -1$ are presented in Fig. 12. By changing D = 0.3 to D = 0.7, the clockwise rotation is horizontally extended and it covers most parts of the cavity so that the counter clockwise rotation is limited to a small area near the cavity's right side. The isotherm contours along the top wall especially near the sink are more crowded than the heat source at the bottom wall for both values of D. Moreover, with changing D = 0.3 to D = 0.7, the congestion of the lines is increased near the heat source. The local entropy contours show that the entropy generation is concentrated along the left and the right walls. The Bejan number is observed along the heat source and in a small area in the middle of the cavity.

Fig. 13 depicts the same purpose and parameters of Fig. 12, but for $\lambda_l = \lambda_r = 1$. On the contrary, with $\lambda_l = -\lambda_r = 1$, the fluid rotates clockwise forming a single-cell circulation near the walls and two weak vortices at the center of the cavity for D = 0.3 and one vortex near the right wall at D = 0.7. The isotherms are mostly vertical in the cavity center, with steeper gradients close to the sink and the left vertical walls upon increasing the value of D. The entropy concentrators look very strong and propagate along both the top and the vertical walls with increasing values of D. The Bejan number shrinks in

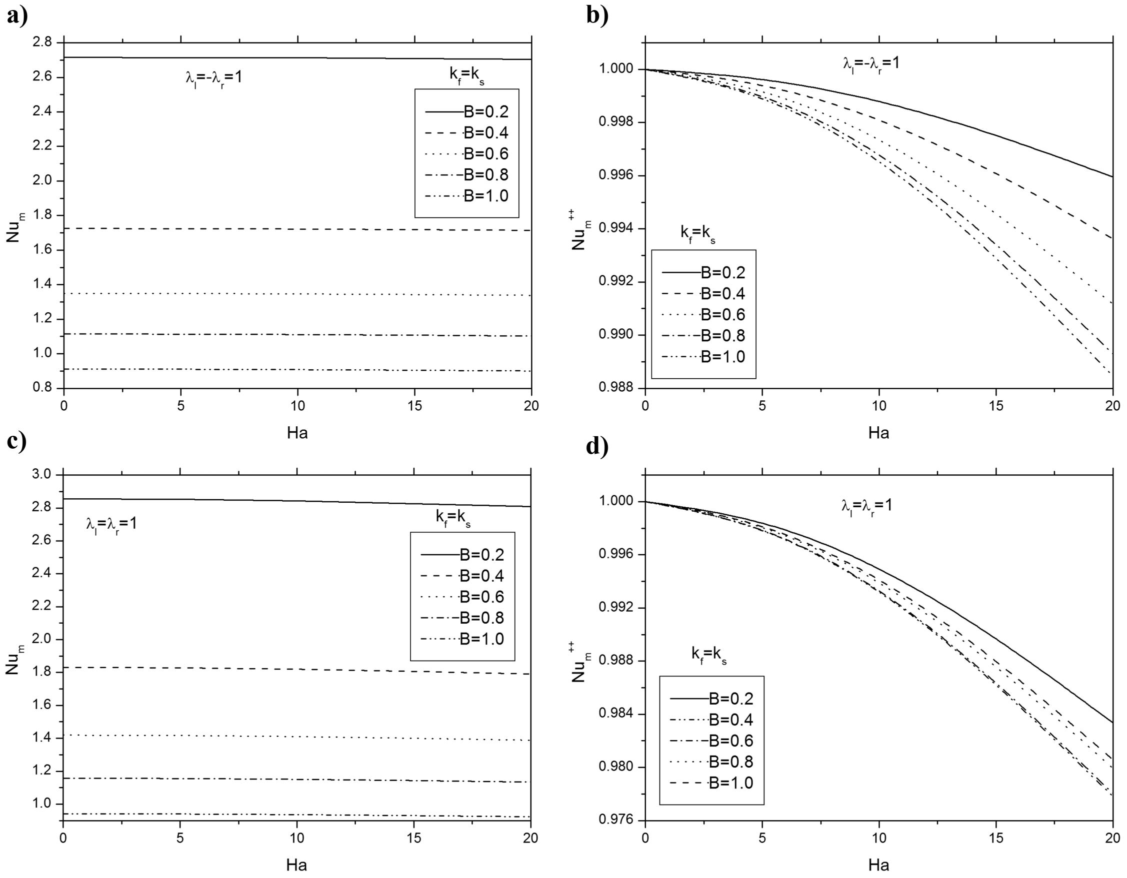

FIG. 9. Variation of the average Nusselt number and Nu_m^{++} for Cu-water with Ha.

the center and along the top wall of the cavity as D is increased from 0.3 to 0.7.

The local Nusselt number ($\mathrm{Nu_s}$) is shown in Fig. 14 for both of $\lambda_l = -\lambda_r = 1$ and $\lambda_l = \lambda_r = 1$. Fig. 14(a) presents $\mathrm{Nu_s}$ for $\lambda_l = -\lambda_r = 1$ at Y = 0. As shown in the isothermal lines in Fig. 12, steeper gradients are seen at the beginning of the heat source for D = 0.3 and at the end of it for D = 0.7, and therefore, $\mathrm{Nu_s}$ shows the maximum value at the beginning of the source for D = 0.3 and at the end of the source for D = 0.7. As shown in Fig. 14(b), the temperature gradient and thus the Nusselt number are increased at the beginning of the sink upon increasing the value of D, but at the end of the sink, a decreasing trend in $\mathrm{Nu_s}$ is experienced as D is increased. Fig. 14(c) illustrates the $\mathrm{Nu_s}$ for $\lambda_l = \lambda_r = 1$ at Y = 0. The Nusselt number at the end of the source is higher than that at the beginning of the source. It is noted that at D = 0.6 and 0.7, the positive temperature gradient (can be seen in the isothermal lines in Fig. 13) leads to negative values of $\mathrm{Nu_s}$ at the beginning of the source. Generally, the increasing trend for $\mathrm{Nu_s}$ at the outset of the source is experienced such as in Fig. 14(b). However, Fig. 14(d) shows that $\mathrm{Nu_s}$ does not have a significant change with increasing values of D at the end of the sink. In the streamlines presented in Figs. 12 and 13, the velocity near the heat sink and source for the two slip cases are different from each other. Generally, the convective heat transfer near the heat sink and source for the case $\lambda_l = \lambda_r = 1$

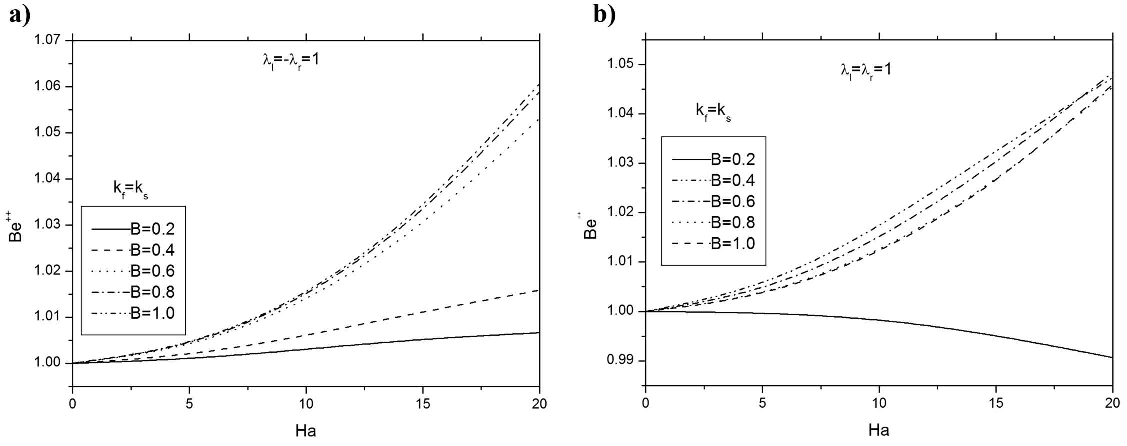

FIG. 10. Variation of the total Bejan number with Ha for (a) $\lambda_l = 1, \lambda_r = -1$ and (b) $\lambda_l = \lambda_r = 1$.

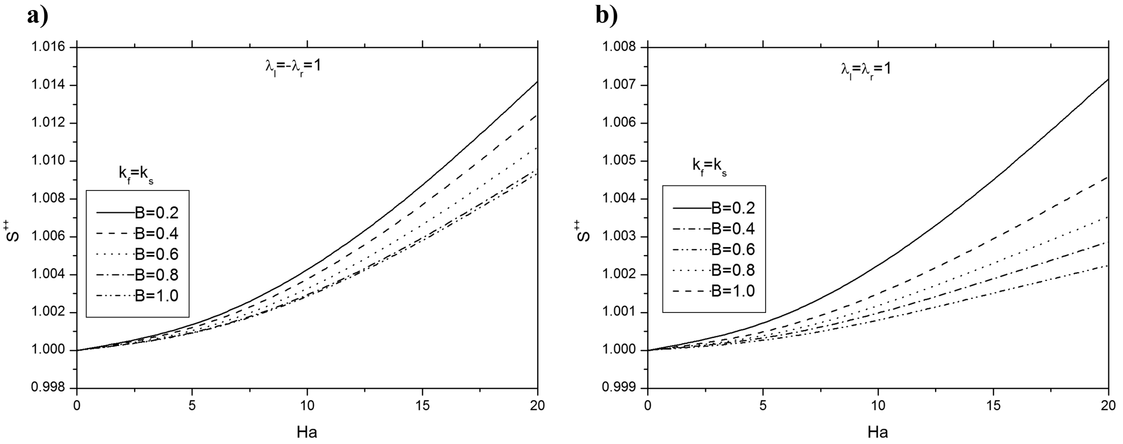

FIG. 11. Variation of the total entropy generation with Ha for (a) $\lambda_l = 1, \lambda_r = -1$ and (b) $\lambda_l = \lambda_r = 1$.

is greater than that for $\lambda_l = -\lambda_r = 1$ because of its velocity, and therefore, it leads to a greater local Nusselt number.

Fig. 15 shows the variation of the average Nusselt number with the nanofluid volume fraction for $\lambda_l = -\lambda_r = 1$ and $\lambda_l = \lambda_r = 1$. For $\lambda_l = \lambda_r = 1$, a continuous decrease in the average Nusselt number is experienced upon enhancing the value of ϕ. This trend also occurs for $\lambda_l = -\lambda_r = 1$. In Figs. 15(a) and 15(c), three distinct groups of curves are visible: D = 0.3 and D = 0.4, D = 0.5 and D = 0.6, and D = 0.7. This is, because of the relatively similar values observed for the local Nu number at Y = 0 and Y = 1 and also its integration in the sink and source domain for the three mentioned groups. The trend of Figs. 15(a) and 15(c) indicates a continuous reduction of the average Nusselt number ratio due to the increase in the nanofluid volume fraction in Figs. 15(b) and 15(d). But the Nusselt number graphs for various values of D in Fig. 15(c) are closer together than those shown in Fig. 15(a), and therefore, the Nusselt number ratio follows the same trend (Figs. 15(b) and 15(d)).

The effect of the volume fraction on the global entropy generation is presented in Fig. 16. Fig. 16(a) shows the S^+ enhancement by increasing the nanofluid volume fraction for all ranges of D. Two stages of the nanofluid effect on S^+ is observed in Fig. 16(b); stage 1 is for low volume fractions where the nanoparticles' actions cause the reduction of S^+, and in stage 2 for high volume fractions, S^+ increases with increasing values of the volume fraction. It should be noted that for all considered values of D, S^+ is less than unity except for D = 0.3 at ϕ = 0.1. As mentioned in Fig. 7, this different behavior between Figs. 16(a) and 16(b) may be because of the different trend in the streamlines and the nanofluid velocity. This reason also may be acceptable for the justification of the

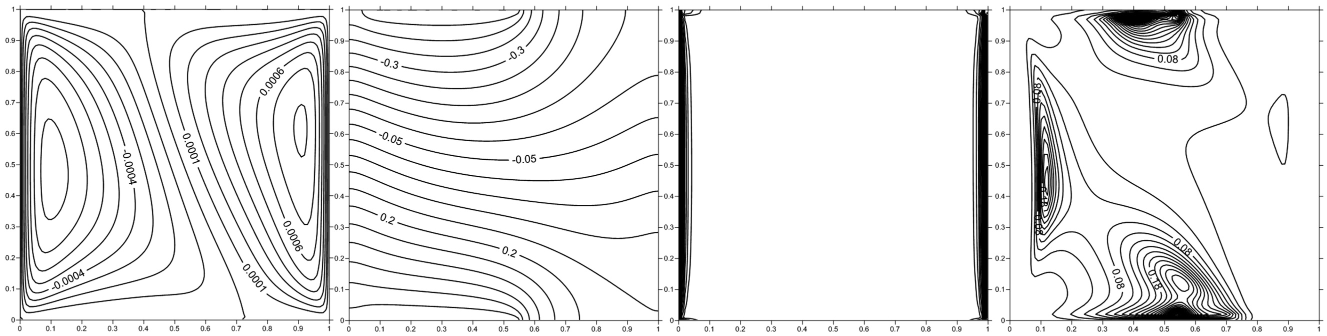

a) D=0.3

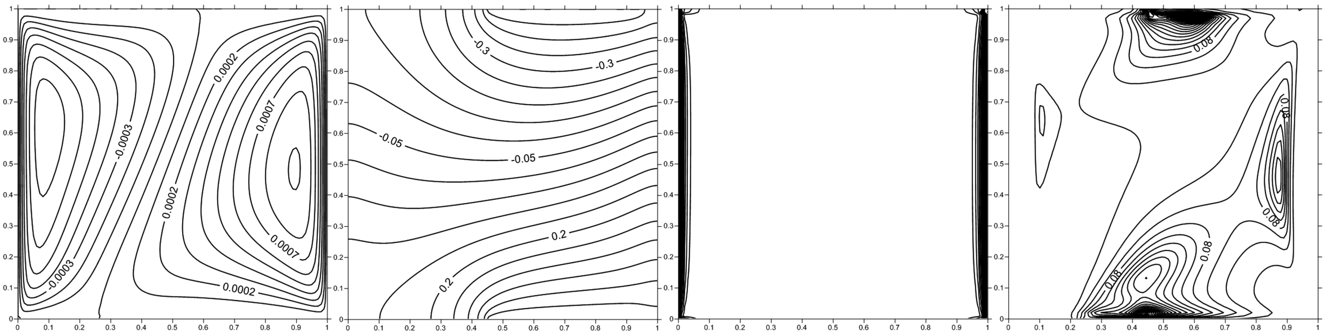

b) D=0.7

FIG. 12. Streamlines, isotherms, local entropy generation, and the local Bejan number for $\phi = 0.05, \lambda_l = \lambda_r = 1$ at (a) D = 0.3 and (b) D = 0.7.

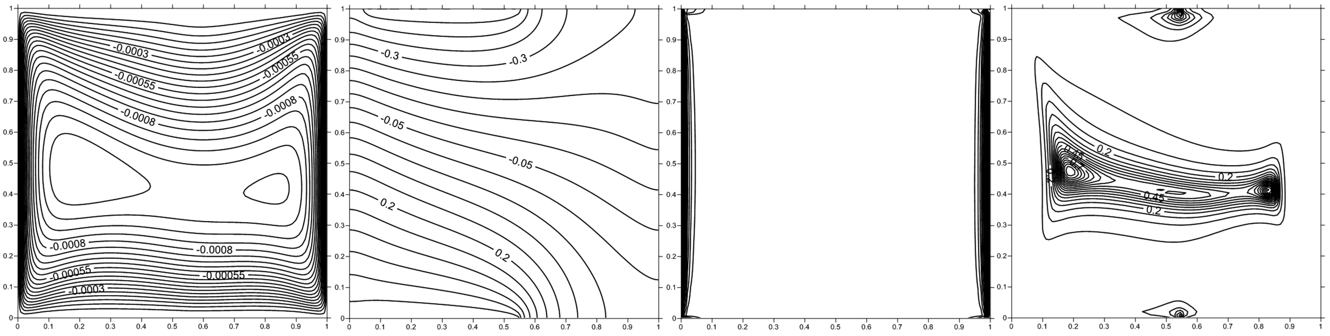

a) D=0.3

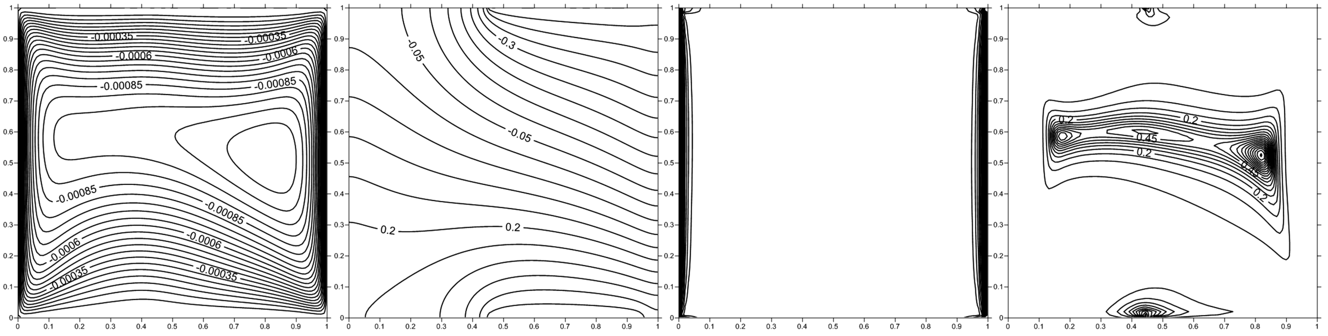

b) D=0.7

FIG. 13. Streamlines, isotherms, local entropy generation, and the local Bejan number $\phi = 0.05, \lambda_l = 1, \lambda_r = -1$ at (a) D = 0.3 and (b) D = 0.7.

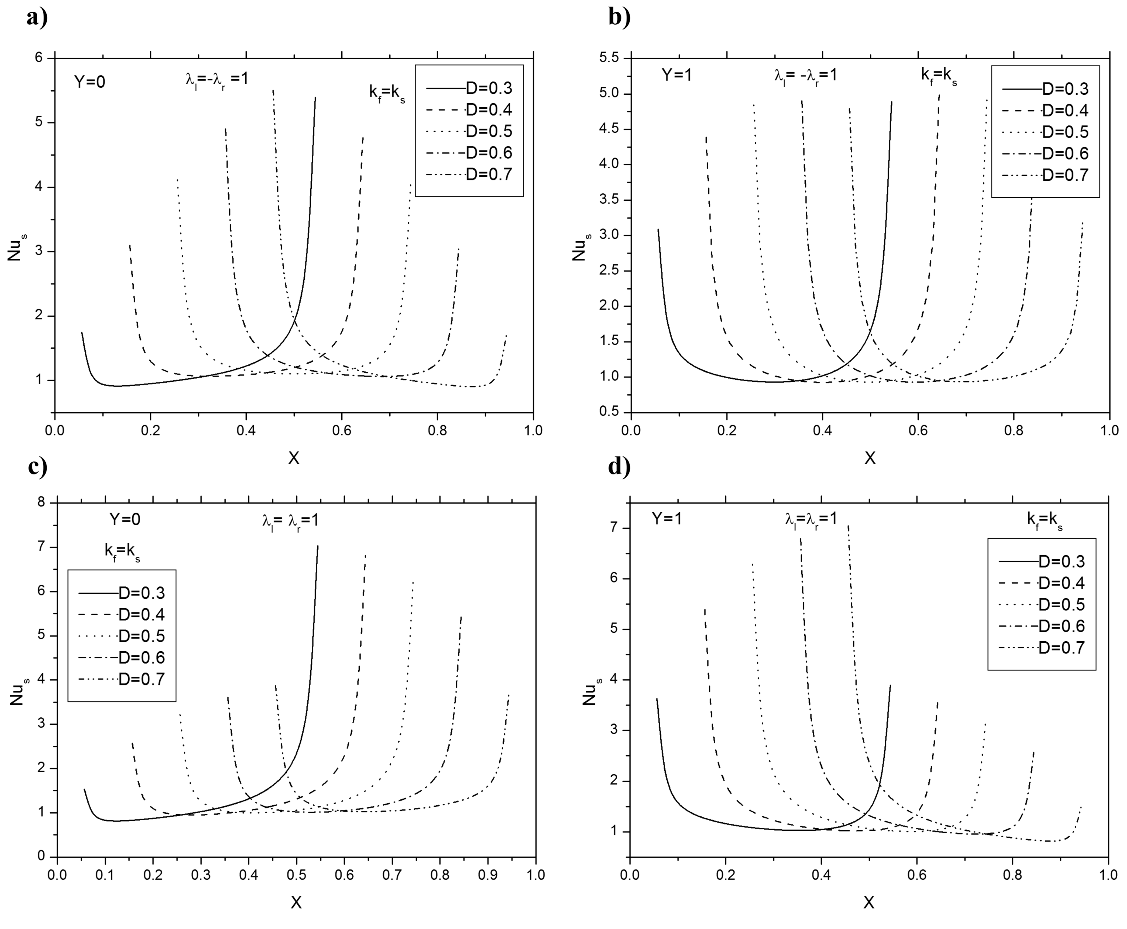

FIG. 14. Profiles of the local Nusselt number for Cu-water for ((a) and (b)) $\lambda_l = 1, \lambda_r = -1$ and ((c) and (d)) $\lambda_l = \lambda_r = 1$.

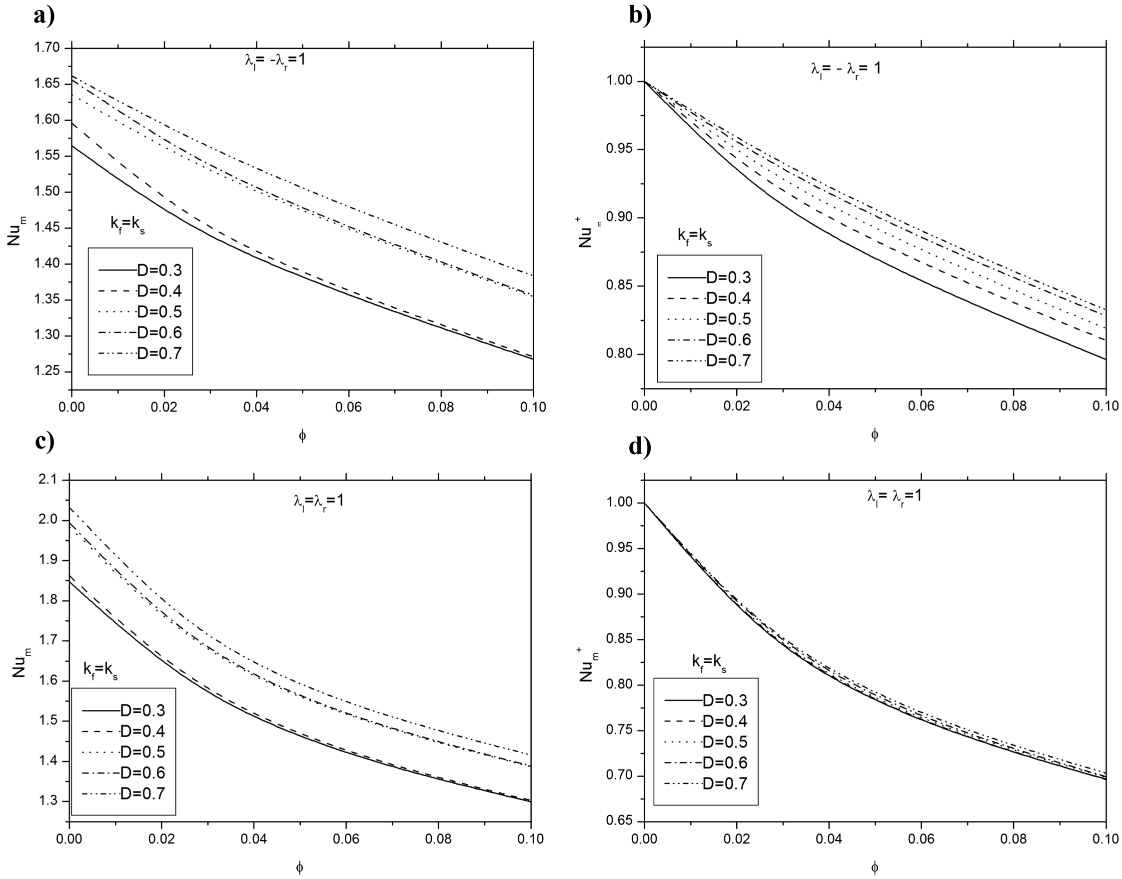

FIG. 15. Variation of the average Nusselt number for Cu-water with ϕ for ((a) and (b)) $\lambda_l = -\lambda_r = 1$ and ((c) and (d)).

difference in behavior shown in Figs. 17(a) and 17(b). The enhancement of the total Bejan number ratio (Be$^+$) through enhancing the volume fraction is presented in Fig. 17.

C. Effect of Richardson number (Ri)

The ratio of natural to forced convection modes is measured by the Richardson number. Its effect is studied by fixing the other dependent parameters at $Ha = 10,\ \phi = 0.05,\ Q = 1$. The Richardson number is related to the Grashof number per square of the Reynolds number, and in this section, Re = 100 and the Richardson number changes by changing the Grashof number.

Fig. 18 shows the effects of the Richardson number on the streamlines, isotherms, local entropy generation, and the Bejan number for $\lambda_l = -\lambda_r = 1$. For Ri = 0.001, the dominance of forced convection can be characterized by the dominance of shear action where two counter rotated vortices exist and each one is guided by a moving wall. Moving up the cores and two weak vortices near the bottom wall due to the enhanced buoyancy effect can be observed in the streamlines for Ri = 10.

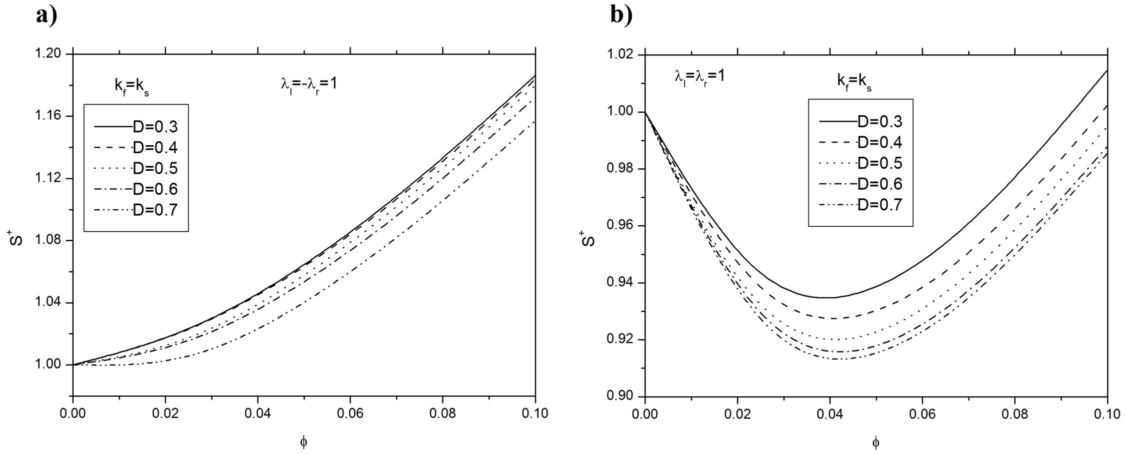

FIG. 16. Variation of the global entropy generation ratio (S$^+$) with ϕ.

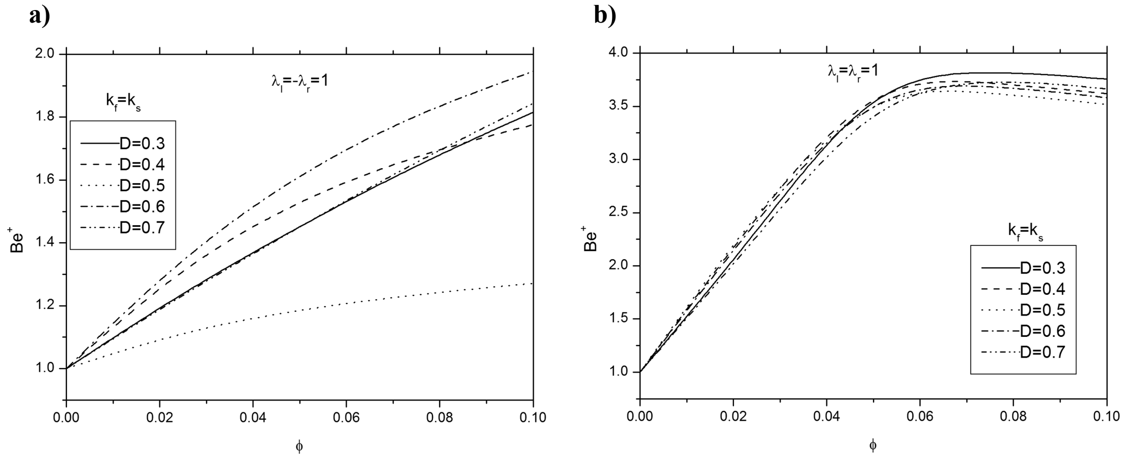

FIG. 17. Variation of the total Bejan number (Be^{+}) with ϕ.

The corresponding isotherms tend to be nearly plumed from the heat source towards the heat sink with isothermal zones localized close to the moving walls and dense isotherms close to the heat sink for Ri = 0.001. For Ri = 10, the isotherms tend to be horizontal in the middle of cavity and with approximately equal isotherms distribution on both sides of the heat sink and source. The formation and growth of the boundary layer and the fluid friction irreversibility lead to more generation of entropy at the top wall for Ri = 10 than Ri = 0.001. The Bejan number is significant near the top and bottom walls for both of the Richardson numbers, and for Ri = 10, it is sensible in the middle of the cavity because of the heat transfer irreversibility.

Fig. 19 indicates the effects of the Richardson number on the streamlines, isotherms, local entropy generation, and the Bejan number for $\lambda_l = \lambda_r = 1$. When the Richardson number is increased from 0.001 to 10, due to the dominance of natural convection, the streamlines are affected by the buoyancy forces and rotate with four weak vortices. By enhancing the thickness of the boundary layers at Ri = 10 and fluid irreversibility as well as heat transfer irreversibility near the walls, the entropy generation is more sensible than it is for Ri = 0.001.

Considering the assumed value of Gr and Re, i.e., Gr = 10^4 and Re = 10^2, the effect of the enhancement of Ha on Nu_m^{++} for Ri = 0.001-1000 is presented in Figs. 20(a) and 20(b). Fig. 20(a) shows a continuous reduction of the Nusselt number by increasing the Hartmann number for Ri = 0.001-1. For Ri = 100-1000, a very smooth decrease is observed in the Nusselt number by increasing the Hartmann number. When

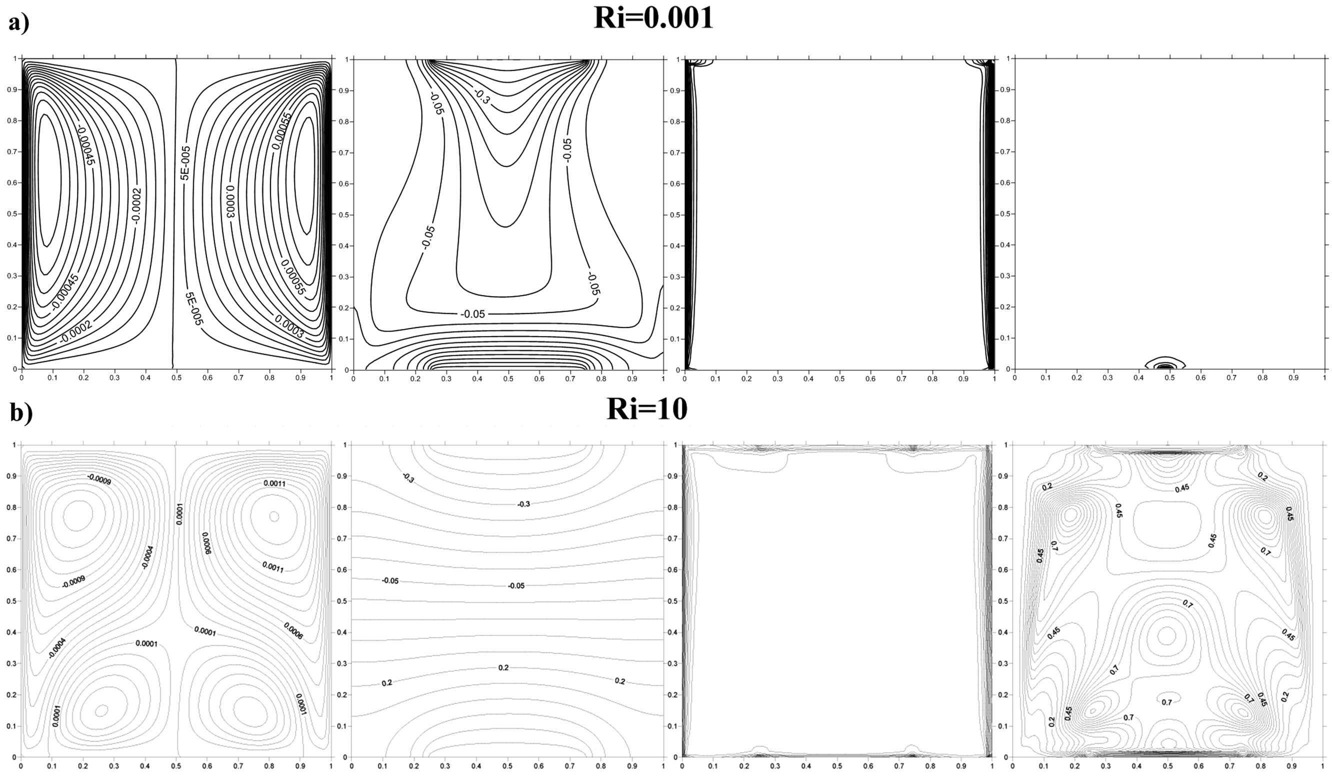

FIG. 18. Streamlines, Isothermal, total entropy generation and the local Bejan number $\varepsilon = 0.5$, $Ha = 10$, $\phi = 0.05$, $B = 0.5$, $D = 0.5$, $\lambda_l = 1$, $\lambda_r = -1$, $Sr = S_l = 1$, $Q = 1$.

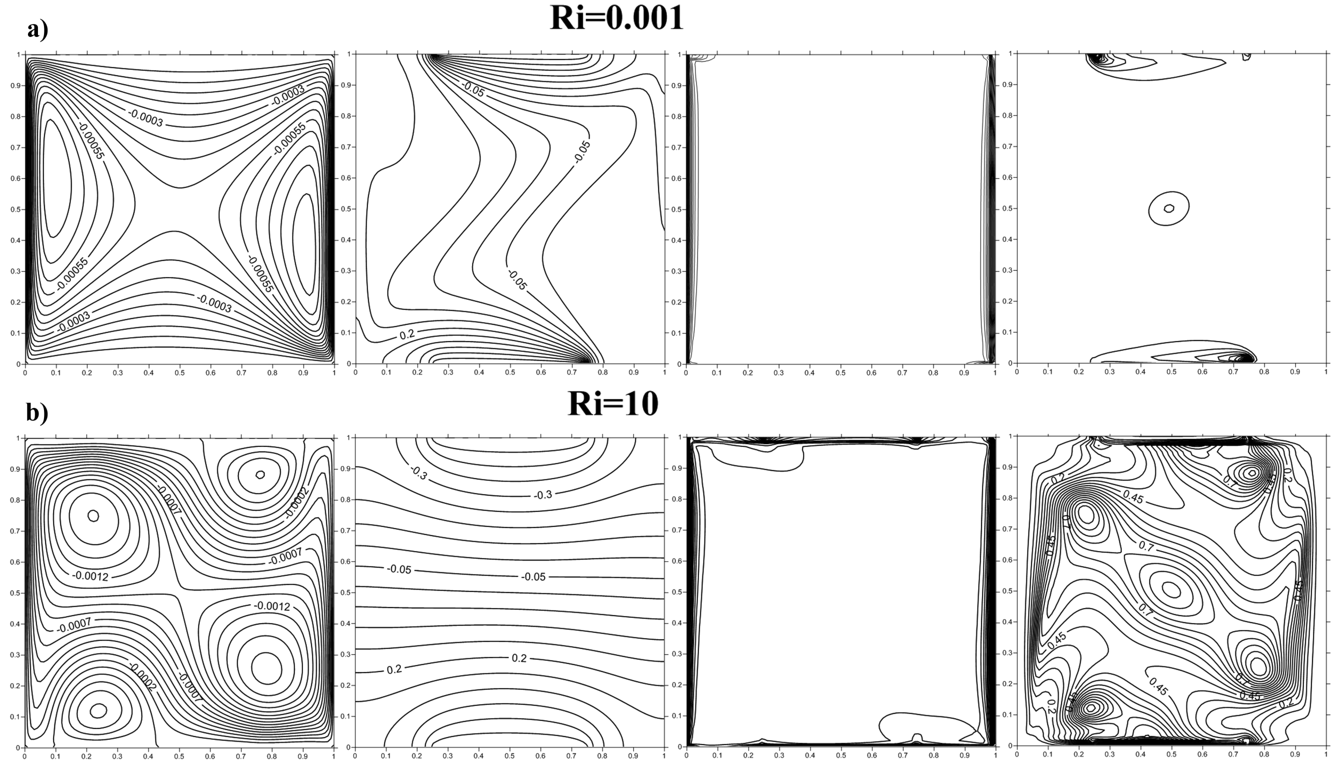

FIG. 19. Streamlines, Isothermal, total entropy generation and the local Bejan number $Ha = 10$, $\phi = 0.05$, $B = 0.5$, $D = 0.5$, $\lambda_l = 1$, $\lambda_r = 1$, $Sr = S_l = 1$, $Q = 1$.

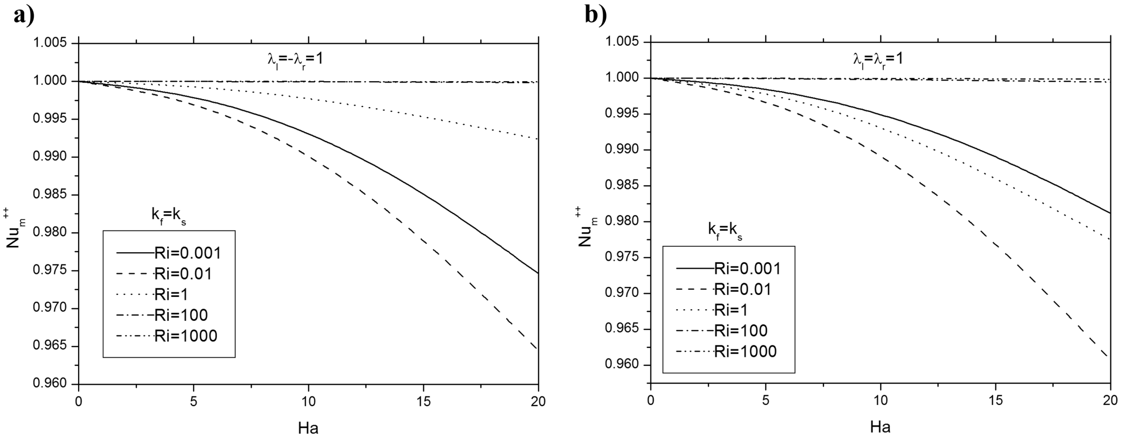

FIG. 20. Variation of Nu^{++} with the Richardson number (a) $\lambda_l = 1, \lambda_r = 1$, (b) $\lambda_l = -\lambda_r = 1$.

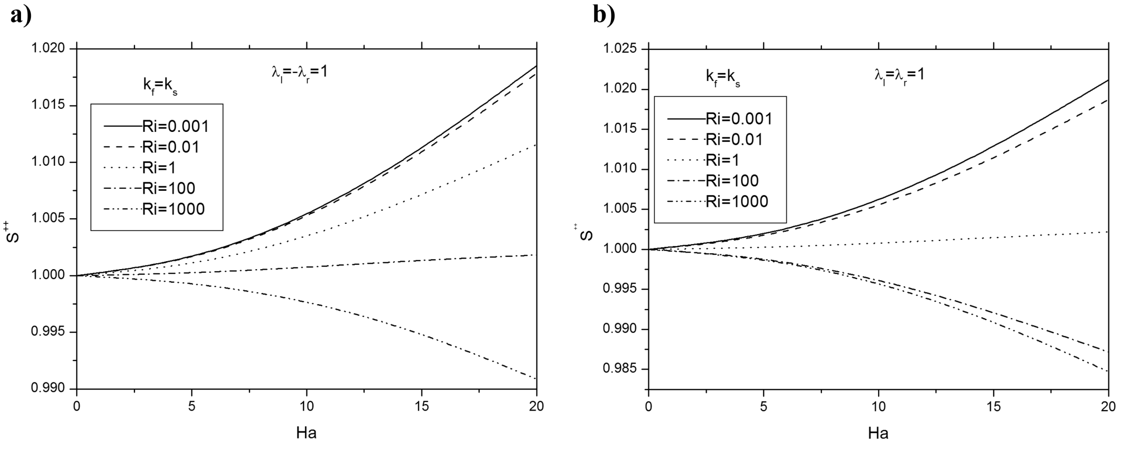

FIG. 21. Variation of S^{++} with the Richardson number (a) $\lambda_l = 1$, $\lambda_r = 1$, (b)$\lambda_l = -\lambda_r = 1$.

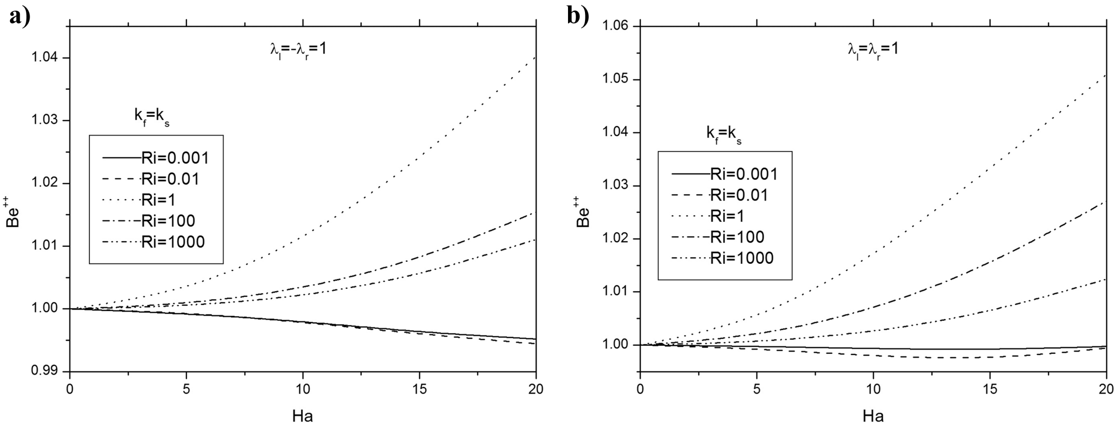

FIG. 22. Variation of Be^{++} with the Richardson number (a) $\lambda_l = 1,\ \lambda_r = 1$, (b) $\lambda_l = -\lambda_r = 1$.

Ri is small, the natural convection regime is strong and there is almost a smooth distribution of velocity and temperature gradients in the cavity. As the Richardson number decreases, the contribution of moving walls in the streamlines and the temperature patterns in the cavity increases. In the case of low values of Ri, for which the moving wall effects are important, there is a strong velocity gradient in the vicinity of the moving side walls. Therefore, the effect of the variation of the magnetic field (Hartmann number) on the Nusselt number is more obvious compared to the large values of Ri, as the Lorentz force is proportional to the velocities in the cavity.

As mentioned, when the Richardson number is large (natural convection dominant regime), the velocities in the entire cavity and next to the side walls are comparatively small. Therefore, the induced magnetic force, which acts proportional to the magnitude of the velocities, is also small. Thus, as it can be seen in Figs. 20(a) and 20(b), Nu^{++} is almost independent of the Hartmann number for the cases with large values of Ri.

The scenario of decreasing Nu_m^{++} by increasing the Hartmann number is obtained in Fig. 20(b) for a low Richardson number and also the smooth decrease of Nu_m^{++} is observed

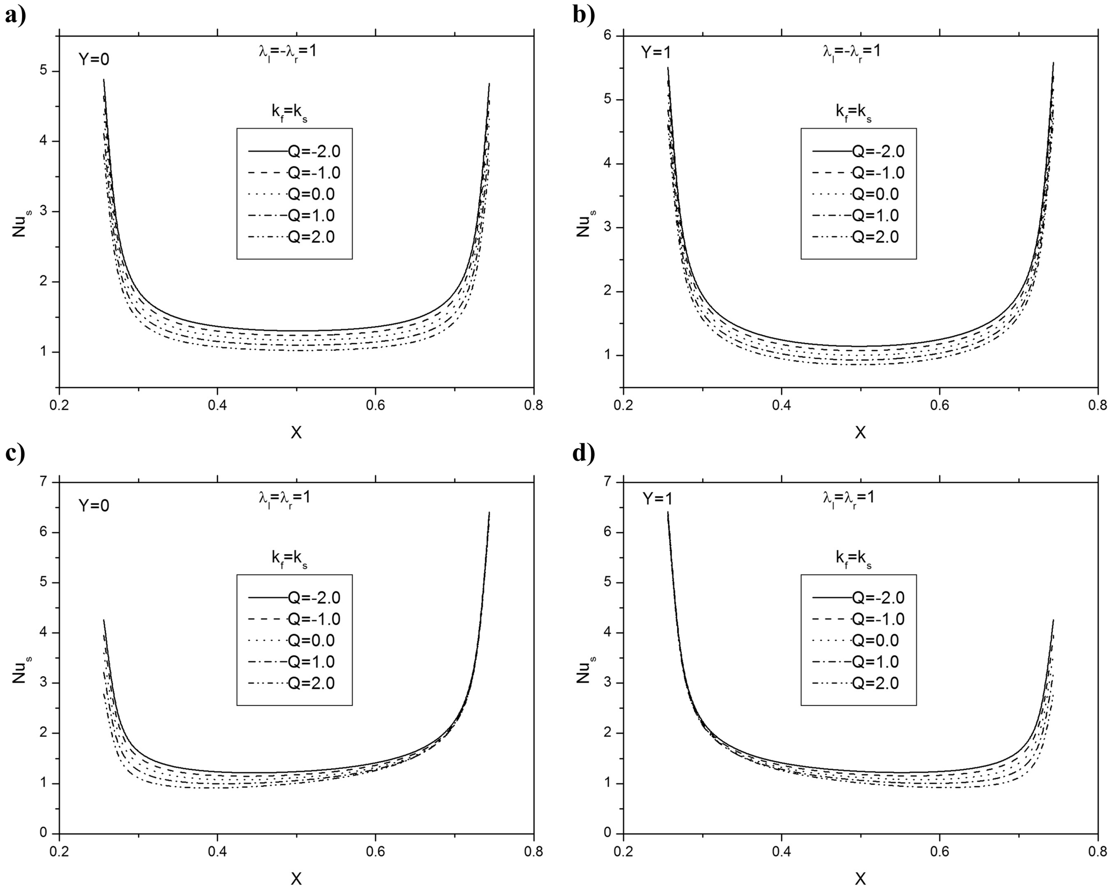

FIG. 23. The local Nusselt number with various values of heat generation ((a) and (b)) $\lambda_l = \lambda_r = 1$ ((c) and (d)) $\lambda_l = -\lambda_r = 1$.

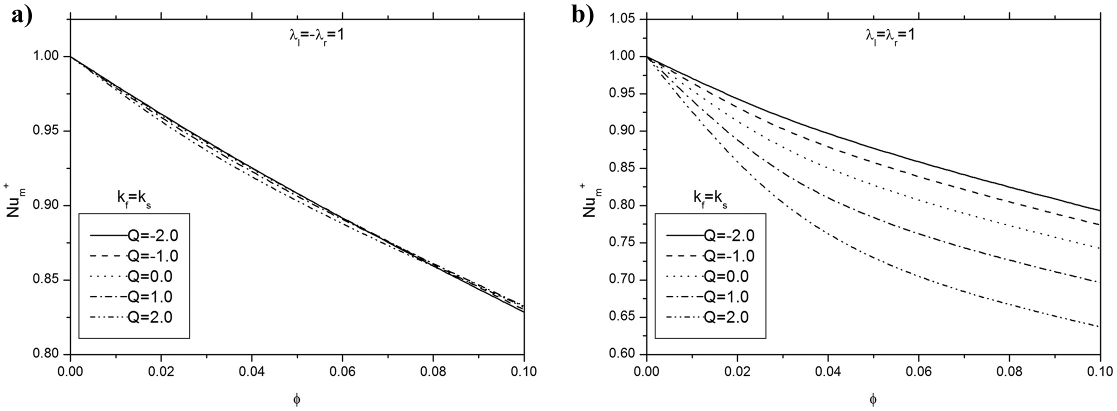

FIG. 24. Variation of the average Nusselt number with various values of heat generation.

for Ri = 100 and 1000 when Ha is enhanced. The magnetic field effect can be clearly observed by the increment of the entropy generation ratio (S^{++}) with increasing values of Ha expect for Ri = 1000 with $\lambda_l = -\lambda_r = 1$ and Ri = 100 and 1000 with $\lambda_l = \lambda_r = 1$ as shown in Fig. 21. Fig. 22 depicts the effect of Ha on Be++ for various values in the range of the Richardson number. Generally, Be^{++} increases with increasing values of Ha for Ri = 0001-1 with $\lambda_l = -\lambda_r = 1$ and $\lambda_l = \lambda_r = 1$.

The local Nusselt number (Nus) is presented in Fig. 23 for Ri = 0.1 and Ha = 10 and various values of Q for both cases of $\lambda_l = \lambda_r = 1$ and $\lambda_l = -\lambda_r = 1$. Figs. 23(a) and 23(b) illustrate Nus for $\lambda_l = \lambda_r = 1$. The negative values of Q indeed show a sink. The increase in the values of Q shows the increase of the internal heat generation in the cavity. The increase of the heat generation tends to increase the overall temperature of the cavity. Hence, the areas next to the hot elements experience a lower temperature difference due to the fact that the temperature of the domain has increased and gets closer to the hot temperature of the wall. However, an increase of the temperature gradient near the cold wall can be expected due to the fact that the generated heat in this region has increased the temperature of the domain. The increase of the temperature next to the cold wall results in a higher temperature gradient at the cold wall and therefore an increase in the Nusselt number. Hence, as seen, in Fig. 23, the increase of Q increases Nus at the cold wall, i.e., $Y = 1$, but it decreases Nus at the hot wall, i.e., $Y = 0$. The trend of the variation of Nus over the hot and cold elements is almost symmetrical in the case of $\lambda_l = \lambda_r = 1$ and unsymmetrical in the case of $\lambda_l = -\lambda_r = 1$. The symmetrical and unsymmetrical trends of behaviors are the result of two smooth circulations in the case of $\lambda_l = \lambda_r = 1$ and one big circulation flow in the case of $\lambda_l = -\lambda_r = 1$. For the case of $\lambda_l = -\lambda_r = 1$, the maximum value of Nus occurs at the beginning of the heat sink and at the end of heat source. The variations of the average Nusselt number ratio with heat generation are displayed in Fig. 24. A continuous reduction of Nu^{++} is observed with the increase in the volume fraction for both of $\lambda_l = -\lambda_r = 1$ and $\lambda_l = \lambda_r = 1$. As observed in the figure, an increment in the heat generation parameter declines the magnitude of the temperature gradient, and thereby, leading to a decrease in the reduced Nusselt number. As mentioned before, the different behaviors in the streamlines and the velocity of the two lid-driven cases cause the differences between Figs. 24(a) and 24(b).

V. CONCLUSION

The effects of the presence of a heat sink and a heat source and their lengths and locations and the entropy generation on mixed convection of a Cu-water nanofluid in a porous media filled in a lid-driven square enclosure with partial slip and subjected to a magnetic field are numerically studied. The effects of the nanofluid volume fraction, Hartmann number and the lengths and locations of the heat sink, and heat source are studied. The results have led to the following concluding remarks:

(1) Increasing the volume fraction of the nanoparticles decreases the convective heat transfer inside the porous cavity for all ranges of the heat sink and the heat source lengths.
(2) The average Nusselt number decreases considerably upon the enhancement of the Hartmann number for all considered range of B.
(3) The enhancement of the total Bejan number ratio (Be^+) through enhancing the volume fraction is seen in the results.
(4) A continuous increment in S^{++} is observed by increasing the Hartmann number for all ranges of B for $\lambda_l = -\lambda_r = 1$ and $\lambda_l = \lambda_r = 1$.
(5) The maximum Nusselt number is seen for B = 0.2 and $\lambda_l = \lambda_r = 1$.
(6) At Ri = 1000, increasing the Hartmann number leads to enhancing the Nusselt number for and this behavior is also seen for Ri = 100 and 1000 with $\lambda_l = \lambda_r = 1$.
(7) The maximum Nusselt number is seen for D = 0.7 and $\lambda_l = \lambda_r = 1$.

[1] T. Basak, S. Roy, P. K. Sharma, and I. Pop, “Analysis of mixed convection flows within a square cavity with uniform and non-uniform heating of bottom wall,” Int. J. Therm. Sci. **48**, 891–912 (2009).
[2] G. Guo and M. A. R. Sharif, “Mixed convection in rectangular cavities at various aspect ratios with moving isothermal sidewalls and constant flux heat source on the bottom wall,” Int. J. Therm. Sci. **43**, 465–475 (2004).
[3] K. M. Khanafer, A. M. Al-Amiri, and I. Pop, “Numerical simulation of unsteady mixed convection in a driven cavity using an externally excited sliding lid,” Eur. J. Mech. B/Fluids **26**, 669–687 (2007).

[4] S. Saha, G. Saha, M. Ali, and Md. Q. Islam, "Combined free and forced convection inside a two-dimensional multiple ventilated rectangular enclosure," ARPN J. Eng. Appl. Sci. **1**(3), 23–35 (2006).

[5] M. D. M. Rahman, M. A. Alim, S. Saha, and M. K. Chowdhury, "A numerical study of mixed convection in a square cavity with a heat conducting square cylinder at different locations," J. Mech. Eng. **ME39**(2), 78–85 (2008).

[6] S. Saha, G. Saha, M. Ali, and Md. Q. Islam, "Combined free and forced convection inside a two-dimensional multiple ventilated rectangular enclosure," ARPN J. Eng. Appl. Sci. **2**(2), 25–36 (2007).

[7] S. U. S. Choi and J. A. Eastman, "Enhancing thermal conductivity of fluid with nanoparticles," in *Developments and Applications of Non-Newtonian Flows*, edited by D. A. Siginer and H. P. Wang (American Society of Mechanical Engineers, New York, 1995), Vol. 231, pp. 99–105.

[8] S. Ahmad and I. Pop, "Mixed convection boundary layer flow from a vertical flat plate embedded in a porous medium filled with nanofluids," Int. Commun. Heat Mass Transfer **37**, 987–991 (2010).

[9] R. K. Tiwari and M. K. Das, "Heat transfer augmentation in a two-sided lid-driven differentially heated square cavity utilizing nanofluids," Int. J. Heat Mass Transfer **50**, 2002–2018 (2007).

[10] D. S. Cimpean and I. Pop, "Fully developed mixed convection flow of a nanofluid through an inclined channel filled with a porous medium," Int. J. Heat. Mass Transfer **55**, 907–914 (2012).

[11] M. Hajipour and A. M. Dehkordi, "Analysis of nanofluid heat transfer in parallel plate vertical channels partially filled with porous medium," Int. J. Therm. Sci. **55**, 103–113 (2012).

[12] M. H. Matin and B. Ghanbari, "Effects of Brownian motion and thermophoresis on the mixed convection of nanofluid in a porous channel including flow reversal," Transp. Porous Media **101**, 115–136 (2014).

[13] D. Srinivasacharya and P. V. Kumar, "Mixed convection along an inclined wavy surface in a nanofluid saturated porous medium with wall heat flux," J. Nanofluids **5**, 120–129 (2016).

[14] B. Jafarian, M. Hajipour, and R. Khademi, "Conjugate heat transfer of MHD non-Darcy mixed convection flow of a nanofluid over a vertical slender hollow cylinder embedded in porous media," Transp. Phenom. Nano Micro Scale **4**, 1–10 (2016).

[15] A. Bejan, "Second-law analysis in heat and thermal design," Adv. Heat Transfer **15**, 1–58 (1982).

[16] A. Bejan, *Entropy Generation Minimization* (CRC Press, Boca Raton, FL, 1996).

[17] M. Sheikholeslami, R. Ellahi, H. R. Ashorynejad, G. Domairry, and T. Hayat, "Effects of heat transfer in flow of nanofluids over a permeable stretching wall in a porous medium," J. Comput. Theor. Nanosci. **11**, 486–496 (2014).

[18] T. W. Ting, Y. M. Hung, and N. Guo, "Entropy generation of viscous dissipative nanofluid flow in thermal non-equilibrium porous media embedded in microchannels," Int. J. Heat Mass Transfer **81**, 862–877 (2015).

[19] M. A. Ismael, T. Armaghani, and A. J. Chamkha, "Conjugate heat transfer and entropy generation in a cavity filled with a nanofluid-saturated porous media and heated by a triangular solid," J. Taiwan Inst. Chem. Eng. **59**, 138–151 (2016).

[20] C. Y. Wang, "Flow over a surface with parallel grooves," Phys. Fluids **15**, 1114–1121 (2003).

[21] Q. He and W.-P. Wang, "Numerical study of the effect of Navier slip on the driven cavity flow," J. Appl. Math. Mech. **89**, 857–868 (2009).

[22] J. Koplik and J. R. Banavar, "Corner flow in the sliding plate problem," Phys. Fluids **7**, 3118–3125 (1995).

[23] M. A. Ismael, I. Pop, and A. J. Chamkha, "Mixed convection in a lid-driven square cavity with partial slip," Int. J. Therm. Sci. **82**, 47–61 (2014).

[24] M. Turkyilmazoglu, "Anomalous heat transfer enhancement by slip due to nanofluids in circular concentric pipes," Int. J. Heat Mass Transfer **85**, 609–614 (2015).

[25] A. Malvandi and D. D. Ganji, "Magnetic field and slip effects on free convection inside a vertical enclosure filled with alumina/water nanofluid," Chem. Eng. Res. Des. **94**, 355–364 (2015).

[26] F. Mabood and A. Mastroberardin, "Melting heat transfer on MHD convective flow of a nanofluid over a stretching sheet with viscous dissipation and second order slip," J. Taiwan Inst. Chem. Eng. **57**, 62–68 (2015).

[27] R. Alizadeh, A. B. Rahimi, and M. Najafi, "Unaxisymmetric stagnation-point flow and heat transfer of a viscous fluid on a moving cylinder with time-dependent axial velocity," J. Braz. Soc. Mech. Sci. Eng. **38**, 85–98 (2016).

[28] R. Alizadeh, A. B. Rahimi, and M. Najafi, "Magnetohydrodynamic unaxisymmetric stagnation-point flow and heat transfer of a viscous fluid on a stationary cylinder," Alexandria Eng. J. **55**, 37–49 (2016).

[29] R. Alizadeh, A. B. Rahimi, R. Arjmandzadeh, M. Najafi, and A. Alizadeh, "Unaxisymmetric stagnation-point flow and heat transfer of a viscous fluid with variable viscosity on a cylinder in constant heat flux," Alexandria Eng. J. **55**, 1271–1283 (2016).

[30] R. Iwatsu, J. M. Hyun, and K. Kuwahara, "Mixed convection in a driven cavity with a stable vertical temperature gradient," Int. J. Heat Mass Transfer **36**, 1601–1608 (1993).

[31] K. M. Khanafer and A. J. Chamkha, "Mixed convection flow in a lid-driven enclosure filled with a fluid-saturated porous medium," Int. J. Heat Mass Transfer **31**, 1354–1370 (1999).

[32] D. A. Nield and A. Bejan, *Convection in Porous Media*, 4th ed. (Springer, 2013).

[33] B. Sreenivasan, P. A. Davidson, and J. Etay, "On the control of surface waves by a vertical magnetic field," Phys. Fluids **17**, 117101 (2005).

[34] M. Sathiyamoorthy and A. J. Chamkha, "Effect of magnetic field on natural convection flow in a liquid gallium filled square cavity for linearly heated side wall(s)," Int. J. Therm. Sci. **49**, 1856–1865 (2010).

[35] M. Sathiyamoorthy and A. J. Chamkha, "Natural convection flow under magnetic field in a square cavity for uniformly (or) linearly heated adjacent walls," Int. J. Numer. Methods Heat Fluid Flow **22**, 677–698 (2012).

[36] K. Khanafer, K. Vafai, and M. Lightstone, "Buoyancy-driven heat transfer enhancement in a two dimensional enclosure utilizing nanofluids," Int. J. Heat Mass Transfer **46**, 3639–3653 (2003).

[37] E. Abu-Nada and A. J. Chamkha, "Effect of nanofluid variable properties on natural convection in enclosures filled with and CuO-EG-water nanofluid," Int. J. Therm. Sci. **49**, 2339–2352 (2010).

[38] J. A. Maxwell, *Treatise on Electricity and Magnetism*, 2nd ed. (Oxford University Press, Cambridge, UK, 1904).

[39] M. Ghalambaz, M. A. Sheremet, and I. Pop, "Free convection in a parallelogrammic porous cavity filled with a nanofluid using Tiwari and Das' nanofluid model," PLoS One **10**, e0126486 (2015).

[40] V. Prasad, F. A. Kulacki, and M. Kayhani, "Natural convection in porous media," J. Fluid Mech. **150**, 89–119 (1985).

[41] H. C. Brinkman, "The viscosity of concentrated suspensions and solution," J. Chem. Phys. **20**, 571–581 (1952).

[42] A. J. Chamkha and M. A. Ismael, "Conjugate heat transfer in a porous cavity filled with nanofluids and heated by a triangular thick wall," Int. J. Therm. Sci. **67**, 135–151 (2013).

[43] S. Mahmud and R. A. Fraser, "Magnetohydrodynamic free convection and entropy generation in a square porous cavity," Int. J. Heat Mass Transfer **47**, 3245–3256 (2004).

[44] A. Bejan, *Convection Heat Transfer* (John wiley & sons, 2013).

[45] S. V. Patankar, *Numerical Heat Transfer and Fluid Flow* (Hemisphere, New York, 1980).

[46] E. Abu-Nada and A. J. Chamkha, "Mixed convection flow in a lid-driven inclined square enclosure filled with a nanofluid," Eur. J. Mech.-B/Fluids **29**, 472–482 (2010).

[47] M. Sheikholeslami, M. G. Bandpy, R. Ellahi, and A. Zeeshan, "Simulation of MHD CuO–water nanofluid flow and convective heat transfer considering Lorentz forces," J. Magn. Magn. Mater. **369**, 69–80 (2014).

[48] A. V. Kuznetsov, "Analytical study of fluid flow and heat transfer during forced convection in a composite channel partly filled with a Brinkman–Forchheimer porous medium," Flow Turbul. Combust. **60**, 173–192 (1998).

[49] C. J. Ho, M. W. Chen, and Z. W. Li, "Numerical simulation of natural convection of nanofluid in a square enclosure: Effects due to uncertainties of viscosity and thermal conductivity," Int. J. Heat Mass Transfer **51**, 4506–4516 (2008).

[50] S. E. B. Maïga, C. T. Nguyen, N. Galanis, and G. Roy, "Heat transfer enhancement in forced convection laminar tube flow by using nanofluids," in *Proceedings of International Symposium on Advances in Computational Heat Transfer III*, Paper CHT-040101, 2004, p. 24.